nature energy

Supplementary information

https://doi.org/10.1038/s41560-024-01556-0

Graphene membranes with pyridinic nitrogen at pore edges for high-performance CO_2 capture

In the format provided by the authors and unedited

Supplementary Information

Table of Contents

Supplementary Notes

Supplementary Note 1. The analysis of CO_2 adsorption and desorption on pyridinic-N-substituted graphene

To understand the interaction between CO_2 and pyridinic-N-substituted pores, CO_2 adsorption-desorption experiments were carried out in near-ambient pressure XPS (NAP-XPS). Primary amine is expected to react with CO_2 and H_2O via zwitterion reactions 1 and 2. The reaction products were $-NHCOO^-$ and $-NH_3^+$ from reaction 1, and bicarbonate ion (HCO_3^-) and $-NH_3^+$ from reaction 2. The strong CO_2 adsorption leads to a stronger peak at ~289 eV (HCO_3^-) in the C1s spectrum of pyridinic-N-substituted graphene (Supplementary Fig. 4). CO_2 and pyridinic N could form into $Py.CO_2$. As a result, pyridinic-N-substituted graphene samples should host $-NH_2$, $-NHCOO^-$, $-NH_3^+$, pyridinic N, $Py.CO_2$, and graphitic N.

$$2(-NH_2) + CO_2 \leftrightarrow -NHCOO^- + -NH_3^+ \quad (1)$$

$$-NH_2 + CO_2 + H_2O \leftrightarrow HCO_3^- + -NH_3^+ \quad (2)$$

$$CO_2 + \text{pyridinic N} \leftrightarrow Py.CO_2 \quad (3)$$

Desorption for removing CO_2 and H_2O

Upon transferring pyridinic-N-substituted graphene samples, previously exposed to the atmosphere, to the NAP-XPS chamber, we carried out XPS measurements to understand the composition of various functional groups. Following this, the sample was heated to 150 ^oC for desorption (chamber pressure: 10^{-9} mbar). The desorption curve shows the intensity of $-NHCOO^-$, $-NH_3^+$/graphitic N, and $Py.CO_2$ reduced from 27.3, 46.5, and 4.9 to 18.8, 35.7, and 0%, respectively (Supplementary Table 1). Meanwhile, the intensity of $-NH_2$ and pyridinic N showed a reverse trend (Fig. 2c and Supplementary Fig. 5). Also, the N1s peak shifted toward low bonding energy, indicating the alteration of chemical bonding due to the desorption (Supplementary Fig. 5d).

CO_2 adsorption-desorption cycle

To measure the CO_2 adsorption of pyridinic-N-substituted graphene, the sample was placed in the XPS chamber filled with 20 mbar of CO_2 at 30 ^oC. Followed by that, CO_2 was evacuated from the chamber, and the XPS measurement was performed. The quantitative analysis shows that the change amount of amine and its derivatives are consistent with the stoichiometry of reaction 1 (Supplementary Fig. 5 and Fig. 2c).

Similarly, the change in Py.CO_2 percentage equaled pyridinic N after CO_2 adsorption. It indicated that the peak at ~403.1 eV is Py.CO_2.

Desorption was carried out at 150 ^oC under vacuum (10^{-9} mbar) in the UHV chamber. After the desorption, the XPS measurement was performed at 30 ^oC. A reversible trend of CO_2 adsorption-desorption via reactions 1 and 3 was observed (Fig. 3f). The result of the 2nd CO_2 adsorption-desorption cycle is similar to the 1st cycle (Fig. 3f and Supplementary Table 1). It showed that pyridinic-N-substituted graphene adsorbs CO_2 via a reversible zwitterion reaction.

The overall chemisorbed CO_2 coverage can be obtained from the total CO_2-adsorbed N functional groups. By summing up the CO_2 adsorbed N-functional groups, the total CO_2-loaded site accounts for 50.9% of the N atoms. Given that the N atoms constitute 9% of the pyridinic-N-substituted lattice, corresponding to N atom density of 3.8×10^{14} cm^{-2}, a CO_2 coverage of 1.7×10^{14} molecule cm^{-2} is estimated.

Supplementary Note 2. Temperature-dependent study on CO_2 desorption

Elevated temperatures (from 30 to 400 ^oC) can further remove H_2O and CO_2 from the graphene lattice (Supplementary Table 2). The intensity of -$NHCOO^-$ and -NH_3^+ from the same sample gradually decreased with increasing temperature (Supplementary Fig. 7). The peaks corresponding to HCO_3^- and -$NHCOO^-$ disappeared nearly completely at 300 ^oC (Supplementary Fig. 7 and 8), indicating that reaction 2 was completely reversed at this temperature. The amount of graphitic N and -NH_3^+ can be deconvoluted by the desorption results (Supplementary Table 2), and the amount of graphitic N ($\leq$ 4.0 %) can be subtracted.

Supplementary Note 3. Effect of NH_3 reaction temperature

NH_3 treatment was carried out with a 7 N of NH_3/CH_3OH solution. The concentration of NH_3 in the gas phase can be estimated by vapor-liquid equilibrium (VLE). The total pressure of NH_3/CH_3OH (P) and the molar ratio of NH_3 in the gas phase (y_1) were extracted from the curve fitting with literature data for the different treatment temperatures (20 and 80 ^oC).[1,2] P and y_1 versus molar composition of NH_3 (x_1) were fitted with a polynomial equation and a linear equation, respectively (Supplementary Fig. 12). Based on the known x_1, the resulting y_1 and P at different temperatures are obtained. (y_1 = 0.94 and y_1 = 0.77 at 20 and 80 ^oC, respectively. P = 0.089 MPa and P = 0.47 MPa at 20 and 80 ^oC, respectively.)

Higher temperature (80 ºC) promoted N doping leading to a higher total N (9 and 20% at 20 ºC and 80 ºC, respectively). Pyridinic N increased by several folds at 80 ºC (Supplementary Fig. 15).

Supplementary Note 4. Estimation of doping level by Raman spectra

Functionalization and doping on graphene lattice can change the Fermi level (electron carrier-density).[3–5] Decreased (increased) Fermi level led by p-type (n-type) doping affects the position of *G*-peak and *2D*-peak and the intensity of the *2D* peak. Therefore, the change of peaks is the indicator of doping concentration dependence. Here are the principles of the Raman shift.[3–5]

1. *G* peak shifts to the right with the increasing doping concentration.
2. I_{2D}/I_G decreases with a higher concentration of electron carrier density.

The Raman mapping (at least 50 points from each sample) were carried out to monitor the doping concentration on the graphene lattice. The *G* and *D* peaks properties, such as intensity, peak position, and full-width half-maximum (FWHM), were fitted with a Gaussian curve after the background of spectra were subtracted (Fig. 4c-e and Supplementary Fig. 13-14).

The blue shift of the *2D* peak indicated that oxidized graphene and pyridinic-N-substituted graphene are p-type doping.[5,6] The *G* peak shift can be used for calculating the doping concentration regardless of the presence of defects on the graphene lattice.[5] The change of Fermi level led by p-type doped graphene can be estimated by equation (1)

$$\Delta E_F = -18\Delta\omega_G - 83 \quad (1)$$

where ΔE_F is expressed in meV for the change of Fermi level due to functionalization and $\Delta\omega_G$, the shift of *G* peak, in cm^{-1}.

The ω_G of pristine graphene, oxidized graphene, and pyridinic-N-substituted graphene (20 and 80 ºC) are 1584, 1588, 1588, and 1592 cm^{-1}, respectively. The obtained ΔE_F are -155.6, -155.6, and -226.0 meV for oxidized graphene, and pyridinic-N-substituted graphene (20 and 80 ºC, Supplementary Table 3).

Supplementary Note 5. Modeling gas transport from pyridinic-N-substituted pores

Pyridinic-N-substituted pores lead to selective and efficient CO_2 transport. To elucidate it, a gas transport model was built as following:

- **CO_2 adsorption on pyridinic-N-substituted 2D pores**

The number of CO_2 molecules adsorbed on pyridinic-N-substituted 2D pores can be expressed by Langmuir single-site isotherm.

$$\frac{q}{q_{max}} = \theta_{pore} = \frac{K_{eq}p}{1+K_{eq}p} \quad (2)$$

where q and q_{max} correspond to the given number of CO_2 molecules adsorbed and the maximum number that can adsorb, respectively. θ_{pore} is the corresponding CO_2 coverage, and K_{eq} is the equilibrium constant for the adsorption of CO_2. p is CO_2 partial pressure.

The CO_2 coverage on pyridinic N was extracted from XPS data measured at different CO_2 partial pressure (Supplementary Fig. 23 and Table 5). K_{eq} (4.4×10^{-4} Pa^{-1}) was extracted by fitting the experimental results at 30 ºC with equation (2). The resulting K_{eq} is consistent with the literature.[7,8]

- **Gas transport through pyridinic-N-substituted 2D pores**

The gas transport through the graphene 2D pore happens via these steps (1) direct impingement of gas molecules to the pore, (2) adsorption of gas molecules to the lattice followed by surface diffusion of the adsorbed molecule to the pore, and (3) translocation of the molecule through the pore.

For small pores in this study, the translocation step is the rate-limiting step.[9] Gas transportation in this mode can be described by a first-order kinetics[9] as follows:

$$P_t = \frac{k_{trans}(\rho)q}{\Delta p} \quad (3)$$

where P_t is the permeance from pyridinic-N-substituted pores, $k_{trans}(\rho)$ is the translocation coefficient for gas molecules passing through pores. ρ indicates that $k_{trans}(\rho)$ is proportional to the pore density, ρ, of such pores. Δp is the pressure differences between feed and permeate.

On the other hand, for a few large pores (e.g., intrinsic defects further expanded by oxidation), the gas molecules would simply effuse through the pore.[10] However, when graphene is supported with a support layer, such as in this work, the transport resistance of effusive graphene pores would be negligible compared to that from the support layer. Therefore, for such pores, the support layer will determine the net transport from the effusive pores.

The NPC support layer is made of rigid porous channels and displays high gas permeance (Supplementary Fig. 18d). The gas transport through NPC support film is in the Knudsen transport regime,[11] and the permeance of NPC can be modeled as follows:

$$P_s = P_{s,n}\, f(T) \tag{4}$$

$$f(T) = \sqrt{T}^{-1} \tag{5}$$

where P_s is the permeance from the NPC membrane. $P_{s,n}f(T)$ is 2×10^5 GPU of CO_2 permeance at 30 °C (Supplementary Fig. 18d).

The net gas permeance is contributed by both types of pores, i.e., small pore, equation (3), and large pores, equation (4), for size-sieving and effusive transport through pyridinic-N-substituted nanopores, respectively. Additionally, the number of CO_2 adsorbed on the pyridinic-N-substituted pores (N_{pore}) can be rearranged as equation (2).

As a result, the total permeance of pyridinic-N-substituted graphene is equal to the sum of the permeance contributed from the selective and support layer. We assume that the permeate pressure is 0 (consistent with using a sweep gas in our experiment where the permeate pressure is low), and the pressure difference is equal to the feed pressure. As a result, it can be expressed as below:

For graphene supported by NPC,

$$P = C_{py}\frac{k_{trans}(\rho)q_{max}K_{eq}}{1+K_{eq}p} + C_s P_{s,n}\sqrt{T}^{-1} \tag{6}$$

where C_{py} and C_s correspond to the fraction of the pores contributing to the size-sieving transport and effusive transport through pyridinic-N-substituted nanopores, respectively.

Given that K_{eq} of CO_2 adsorbed on pyridinic N was extracted from the XPS data, the correlations between the fraction of size-sieving transport and the gas permeance can be extracted (Fig. 5e and Supplementary Table 10) by plugging the data into the equation (6) for the curve fitting.

The resulting C_{py} shows a linear relation with the CO_2 permeance (Fig. 6a and Supplementary Table 10), indicating that the permeance is determined by the ratio of size-sieving transport. Additionally, the CO_2/N_2 separation factor increases with the increasing C_{py}. It shows that transportation through the pyridinic-N-substituted 2D pores leads to efficient CO_2 transport. The translocation coefficient determined by porosity also increases with the increasing CO_2 permeance[9] (Supplementary Fig. 24).

- **Temperature-dependent CO_2 transport**

K_{eq} can be fitted with Van 't Hoff equation to obtain the adsorption energy, ΔH_{ad}, as per equation (7).

$$\ln K_{eq} = \frac{-\Delta H_{ad}}{RT} + \frac{\Delta S}{R} \quad (7)$$

where ΔS is the entropy change upon CO_2 adsorption.

Given a good prediction of CO_2 permeance with our transport model, equation (6), we extracted K_{eq} at three different temperatures (20, 60, and 100 ºC) based on *p*-dependent permeation data. For this, CO_2 permeation was measured at the three temperatures with p varying from 12 mbar to 400 mbar (Supplementary Table 11). The obtained K_{eq} at the three temperatures are listed in Supplementary Table 12. By plugging the obtained K_{eq} into equation (7), ΔH_{ad} was obtained as the slope in a plot of $\ln K_{eq}$ with $\frac{1}{RT}$ (Supplementary Fig. 25a). The resulting adsorption energy ΔH_{ad} is 25.2 kJ mole^{-1} (0.26 eV, Supplementary Table 12), in agreement with the theoretical prediction on the binding energy of CO_2 with pyridinic N in the range of 0.20 – 0.27 eV.[12–15] The fitting of K_{eq} with temperature based on p dependent permeation data also outputs $k_{trans}(\rho)$ (Supplementary Table 12). Based on this, activation energy, E_{act}, for translocation can be extracted per equation (8):

$$k_{trans}(\rho) = A_{trans}\exp(\frac{-E_{act}}{RT}) \quad (8)$$

where A_{trans} combines pre-exponential factor for the Arrhenius term and density of CO_2-sorbed pores. Given that q_{max} is a constant, the resulting activation energy (34.8 kJ mole^{-1}) was obtained as the slope in a plot of $q_{max}k_{trans}(\rho)$ with $\frac{1}{RT}$ (Supplementary Fig. 25b and Table 12).

Since the apparent activation energy can be expressed as equation (9):

$$E_{act-app} = E_{act} + \Delta H_{ad} \quad (9)$$

By plugging the ΔH_{ad} and E_{act} obtained from equation (8 and 9), respectively, the resulting $E_{act-app}$ (9.6 kJ mole^{-1}) is low due to the strong CO_2 adsorption of pyridinic N-substituted pores. The result is similar to the temperature-dependent gas permeation measurement for the membranes with high oxidation time ($E_{act-app}$ is close to 0 kJ mole^{-1}, (Fig. 6b, Supplementary Fig. 26, Supplementary Note 6). It supports that the gas transportation through the 2D pores is strongly influenced by the pyridinic N.

Supplementary Note 6. The apparent activation energy for gas transport

Gas transport across 2D pores of graphene, when the pore size is concomitant to the size of the gas molecule, takes place by a temperature-activated transport mechanism[16]. By fitting the temperature-dependent gas flux with an Arrhenius relationship, the apparent activation energy, $E_{act-app}$, for gas transport can be extracted.

$$Flux = A_0 \exp(\frac{-E_{act-app}}{RT}) \quad (10)$$

where A_0 combines the pre-exponential factor for the Arrhenius term and the density of gas-occupied pores. $E_{act-app}$ is essentially the sum of the activation energy (E_{act}) for gas molecules to translocate the pores and the adsorption energy (ΔH_{ad}) of gas molecules on the graphene pore.

Supplementary Note 7. Techno-economic model for a double-stage membrane process

The carbon capture penalty values reported in the manuscript are calculated via a techno-economic model, that can simulate, design, and optimize multi-stage membrane processes for gas separation. The tool can simulate various configurations, i.e., single-, double- or triple-stage, with either compression of the feed or permeate under vacuum or combinations of feed compression and permeate under vacuum.

The design of the process is based on the minimization of the error between the calculated and the target values of recovery and purity of the main component (i.e., CO_2 for post-combustion carbon capture), by varying the design variables, i.e., the areas of the membrane stages for given pressures. The tool can also find optimal sets of pressures to minimize the overall capture penalty, via grid optimization. The model has been already presented in previous work.[17] To simulate and design the process with specific membranes, the model requires as inputs the values of CO_2 permeance, CO_2/N_2 selectivity, CO_2/O_2 selectivity, and CO_2/H_2O selectivity.

The multi-stage membrane process is simulated as the combination of two or more single membrane stages. The model implemented for a membrane stage is based on previous models reported in the literature, referring to asymmetric polymeric membranes and the main assumptions are: (i) no mixing in the supporting layer on the permeate side; (ii) negligible concentration polarization; (iii) constant pressure in the permeate and the feed side; (iv) isothermal process.[18,19] For this work, all membrane stages are simulated with a cross-plug flow arrangement, as this is most often used in gas separation units.[20]

The membrane area is discretized along the length (z-axis) in a certain number of membrane elements. The model starts from the estimation of transmembrane fluxes for each species and for each discretization element, as a result of the partial pressure driving force. The transmembrane flux J [mol ($m^{-2}s^{-1}$)] for a generic component *i* is then expressed as:

$$J_i = \boldsymbol{P}_i \left(P_i^f - P_i'^p\right) = \boldsymbol{P}_i \left(P_{feed}\, x_i^f - P_{perm}\, x_i'^p\right) \quad (11)$$

where $\boldsymbol{P}_i$ is the permeance [$molm^{-2}s^{-1}Pa^{-1}$)] of the component *i*; P_i^f is the partial pressure of component *i* in the feed side, given by the product of the total pressure P_{feed} and the fraction x_i^f of component *i* in the feed. $P_i'^p$ is the partial pressure in the permeate side right after the selective membrane layer, given by the product of the total pressure P_{perm} and the fraction $x_i'^p$ of component *i* in the permeate side.

Then, the model estimates the total flux through the membrane as the sum of the fluxes of each component and applies mass balances to calculate the variation of concentration and flow rates along the feed and the permeate channel. In particular, for a generic discretization element z[th] along the membrane length with membrane area dA, the entering feed flow rate $(Q_f)_z$ (mol s^{-1}) is converted into a retentate flow rate $(Q_r)_z$ (feed to the following element) and into a permeate flow rate that is collected on the other side of the membrane. The total mass balance and the mass balance on component *i* are reported below:

$$(Q_f)_z = (Q_r)_z + (J_{tot} dA)_z \tag{12}$$

$$(Q_f\, x_i^f)_z = (Q_r\, x_i^r)_z + (J_i dA)_z \tag{13}$$

According to the hypothesis of cross-plug flow, the permeate streams generated in each discretization element are not mixed along the length of the unit. The total permeate stream $Q_{p,out}$ produced in the membrane stage is given by the sum of the transmembrane fluxes generated in each discretization element, as reported in equation (14 and 15).

$$Q_{p,out} = \sum_z (J_{tot} dA)_z \tag{14}$$

$$Q_{p,out}\, x_i^p = \sum_z (J_i dA)_z \tag{15}$$

To simulate a double- or triple-stage membrane process, the model for the single stage is incorporated into a modeling framework where proper connections between the stages are defined depending on the configuration. In most cases, a double-stage process where the retentate of the second stage is recycled and mixed with the inlet feed results in the most economically competitive. For this configuration, an iterative procedure has been set up to take into account the variation of the feed flow rate and composition when the feed is mixed with the 2[nd] retentate. Once the process is designed, the main economic figures are estimated via the economic model that takes membrane area and power requirements to calculate capital and operating costs. The capital costs include the direct costs for membrane (which accounts also for housing, piping, and instrumentation), for vacuum pumps (specific direct cost of 870 \$/kW, published in 2016[22] and updated via the index CEPCI) and of compressors (specific direct cost of 1000 \$/kW, published in 2016 and updated via the index CEPCI).[22] We consider two reference costs of membranes, a conservative estimation of 500 \$/m^2 and a more recent estimate of 100 \$/m^2 based on improved manufacturing processes of graphene membranes at a larger scale. Beyond the direct costs for the equipment, the capital costs include the indirect costs, calculated as 14% of the total direct costs in line with previous works,[22,23] and the contingency costs, given by 15% (project contingency) plus 20% (process contingency) of the sum of equipment and indirect

costs.[23] The capital costs are annualized via a capital charge factor of 0.125 to estimate the CAPEX [$/y].[23] The operating costs (OPEX [$/y]) are given by the cost for electricity (specific cost of 0.05 $/kWh), for membrane replacement (every 5 years with a cost of the sheet of one fifth of the specific direct cost of membranes)[22], and by the fixed operating costs (i.e., the cost for maintenance and for labor), calculated as 7% per year of the sum of equipment and indirect costs.[21] The overall capture penalty [$/ton] is given by the sum of CAPEX and OPEX, divided by the total amount of CO_2 recovered per year.

The values of carbon capture penalty from concentrated feed (10-20% CO_2) reported in the manuscript are calculated with CO_2 permeance of 8900 GPU and CO_2/N_2 selectivity of 85, in line with the experimental results. The other values of selectivity are equal to 1 for CO_2/H_2O and 12.6 for CO_2/O_2.[24] The optimal configuration to recover 90% CO_2 at 95% purity from a concentrated feed (CO_2 partial pressure of 200 mbar) is a double-stage membrane process with the recycle of the second retentate and with partial pressure driving force generated only via vacuum in the permeate (Supplementary Fig. 33). This is because membranes are highly permeable and the effect of membrane area increase without feed compression on the total capture penalty is negligible. The optimal pressures in the permeate channels (with ambient pressure in the feed channel) are 0.04 bar in the first stage and 0.25 in the second stage. The specific membrane area is 1.4×10^3 m^2 s kg^{-1}, the specific energy consumption is 0.69 MJ kg^{-1} and the total capture penalty is 19.6 $/ton with membrane cost of 100 $/$m^2$ and 25.9 $/ton with 500 $/$m^2$.

With the same pressure configuration and CO_2 partial pressure of 135 mbar (typical CO_2 concentration of 13.5% in coal-based power plant flue gas), the specific membrane area is 2.2×10^3 m^2 s kg^{-1}, specific energy consumption is 0.81 MJ kg^{-1} and total capture penalty is 23.8 $/ton with membrane cost of 100 $/$m^2$ and 33.5 $/ton with 500 $/$m^2$.

In the case of low-concentration feed (CO_2 partial pressure of 10 mbar), we simulate the membrane process with improved performances in line with the experimental results. As the CO_2 concentration in the feed decreases, CO_2 permeance and CO_2/N_2 selectivity are found to increase thanks to the capability of the membranes to selectively adsorb CO_2 even in diluted conditions (see Supplementary Table 10). For this reason, the CO_2 permeance is taken equal to 10000 GPU and the CO_2/N_2 selectivity is 1000 in the first stage (very low concentration) and 100 in the second (higher concentration). With these membrane properties, the selected layout to target 90% CO_2 recovery and 95% purity (shown in Supplementary Fig. 34) presents a double stage without recycle (the concentration and the flow rate of the second retentate are low and would not contribute significantly to increasing driving force). As the feed is assumed to contain water vapor with a relative humidity of 50% (H_2O partial pressure of 17 mbar), most of the water vapor from the

1st permeate is condensed between the first and the second stage and this helps to increase CO_2 concentration before the second stage. Also, in this case, it is more feasible to generate vacuum in the permeate rather than compressing the feed, because the feed flow rate is much larger than permeate flow rate. The optimal permeate pressures, in this case, are 0.005 bar in the first stage and 0.1 bar in the second stage. The obtained specific membrane area is 3.3×10^4 m^2 s kg^{-1}, the specific energy consumption is 1.52 MJ kg^{-1} and the total capture penalty is 76.2 \$/ton with membrane cost of 100 \$/m^2 and 220 \$/ton with 500 \$/m^2.

We performed sensitivity analysis for each of the three case studies, by varying some relevant economic parameters to assess their impact on the overall capture penalty. First, we varied the specific cost of membranes from near 0 to 1000 \$/m^2 (Supplementary Fig. 35) and we found a stronger dependency of the capture penalty on membrane cost for decreasing inlet feed concentrations. This is because larger membrane areas are needed when the inlet concentration is lower, for the same purity and recovery targets. Then, we varied the specific cost of vacuum pumps (current value), the indirect cost factor, and the specific cost of energy within a range of deviation from the base case from -100% to +100%. We carried out these analyses with a membrane cost of either 100 \$/m^2 or 500 \$/m^2 (Supplementary Fig. 36).

In general, for a given membrane cost, the cost of energy impacts the most the capture penalty, followed by the specific cost of vacuum pumps and the indirect cost factor. This last term has a very limited impact, as it gives a maximum variation of capture penalty of around 8%. Another general observation is that the range of capture penalty variation enlarges when the membrane cost is lower (100 \$/m^2) because the capture penalty is dominated by the investment cost of membranes in the case of the specific membrane cost of 500 \$/m^2. This is particularly evident in the case of 1% CO_2 feed, where the variation of capture penalty with any of the three economic parameters is almost negligible with the high membrane cost. The sensitivity to vacuum pump cost and energy cost increases with membrane cost of 100 \$/m^2, as the maximum estimated variation of capture penalty with 1% CO_2 feed is around 23% and 28%, respectively.

On the other hand, the systems with 13.5% and 20% CO_2 feed have similar behavior: the maximum capture penalty variation connected to energy cost goes from 36% with membrane cost of 500 \$/m^2 to 48% with membrane cost of 100 \$/m^2, and the one connected to vacuum pump cost from 28% with 500 \$/m^2 to 39% with 100 \$/m^2.

Supplementary Figures 1-39

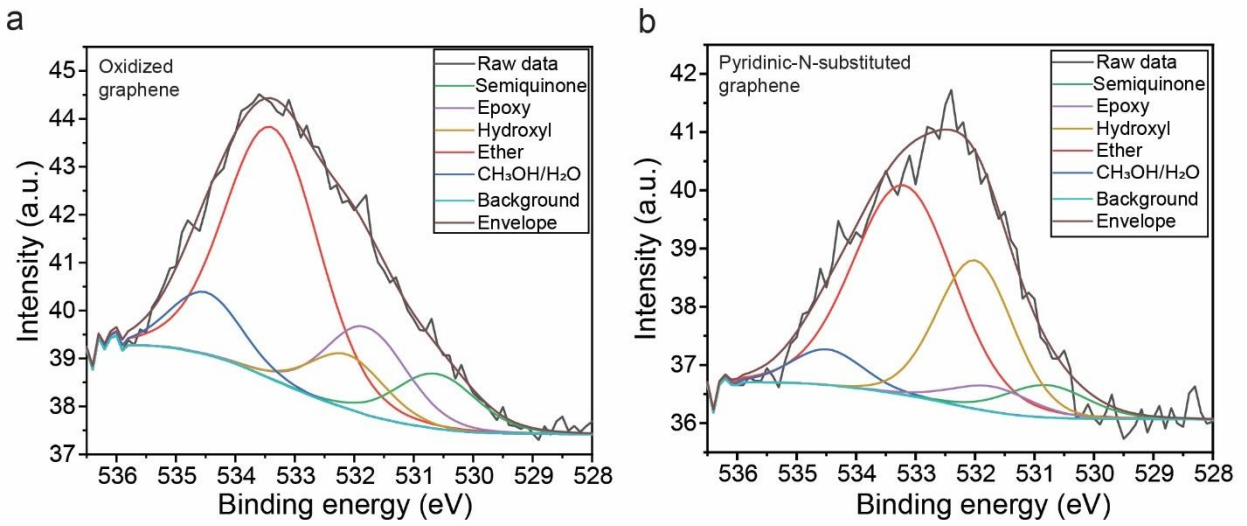

Supplementary Fig. 1. O1s XPS spectra from (a) oxidized sample (precursor for NH_3 reaction), and (b) pyridinic-N-substituted sample prepared by reaction with NH_3 at 20 ºC. The substrate was highly-oriented pyrolytic graphite (HOPG) to avoid complications from residues on transferred graphene which often makes O1s analysis difficult.

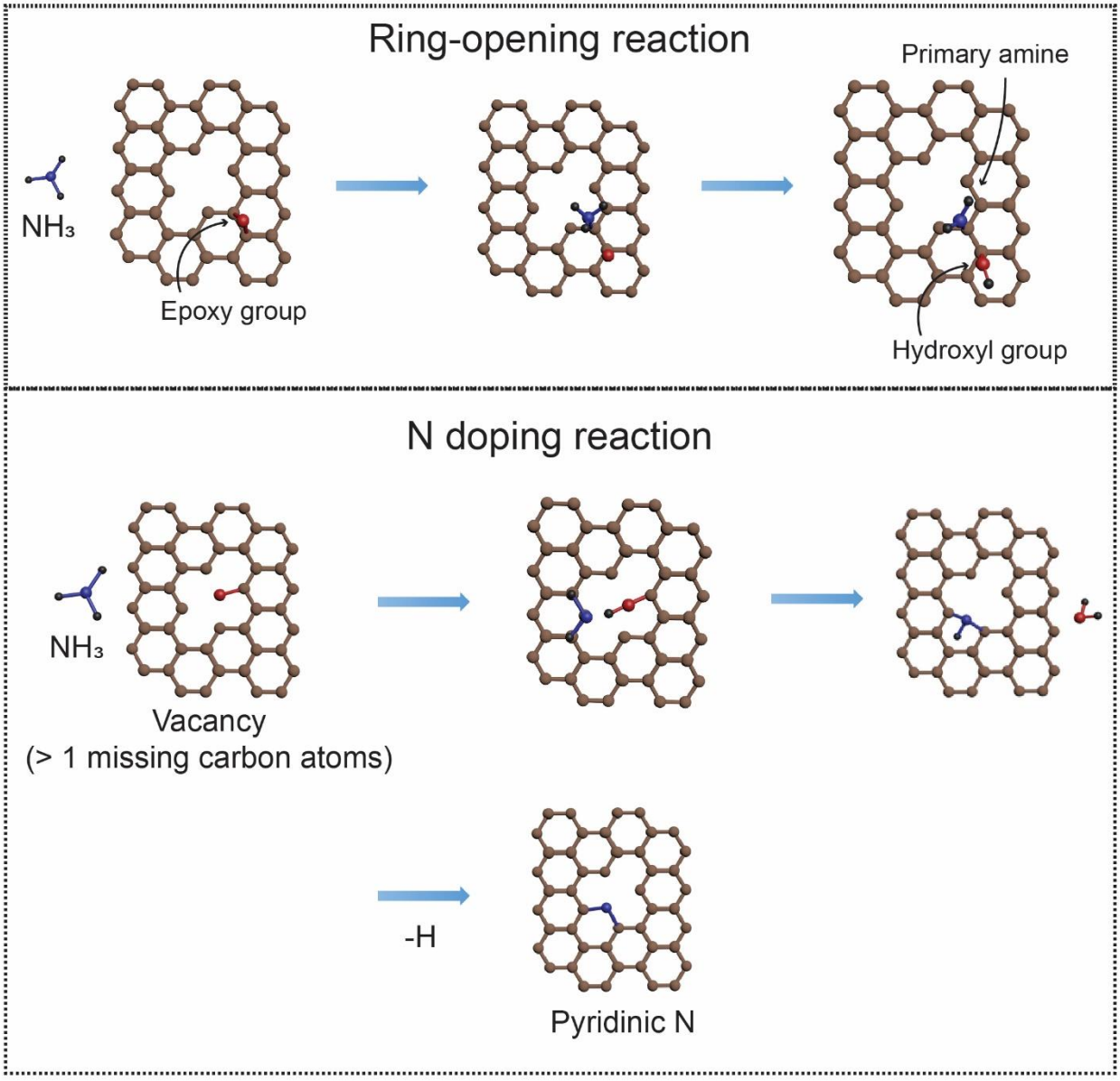

Supplementary Fig. 2. Reaction mechanism for NH_3 with semiquinone group at the pore edge to yield pyridinic N based on the theoretical literature on reaction mechanism.[25,26]

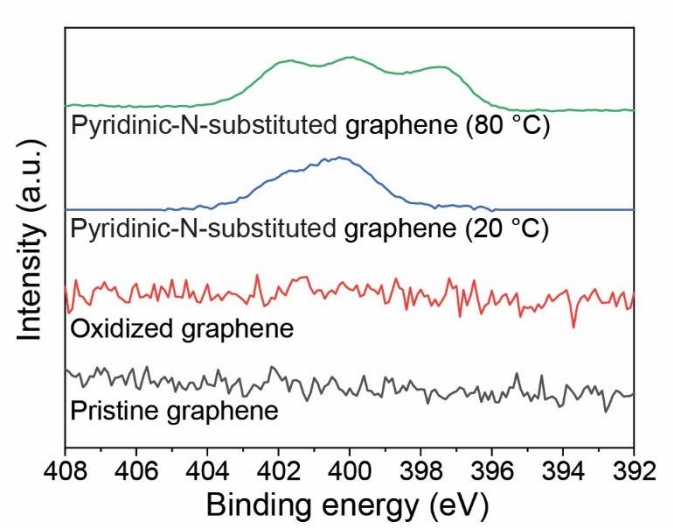

Supplementary Fig. 3. N1s XPS spectrum of pristine graphene, oxidized graphene, and pyridinic-N-substituted graphene using 20 ºC and 80 ºC NH_3 treatment.

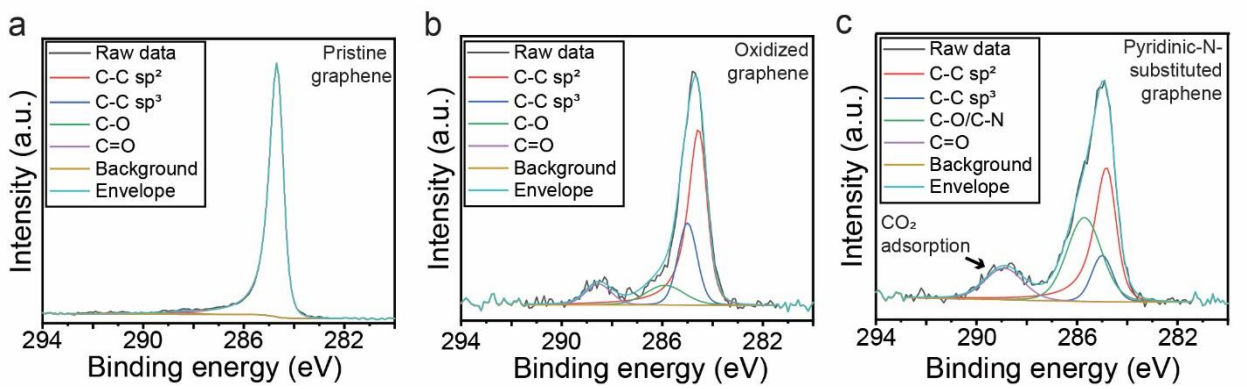

Supplementary Fig. 4. C1s XPS spectra from pristine graphene (a), O_3 treated graphene at 20 ºC for 1 h (b), and pyridinic-N-substituted graphene treated at 20 ºC for 24 h (c).

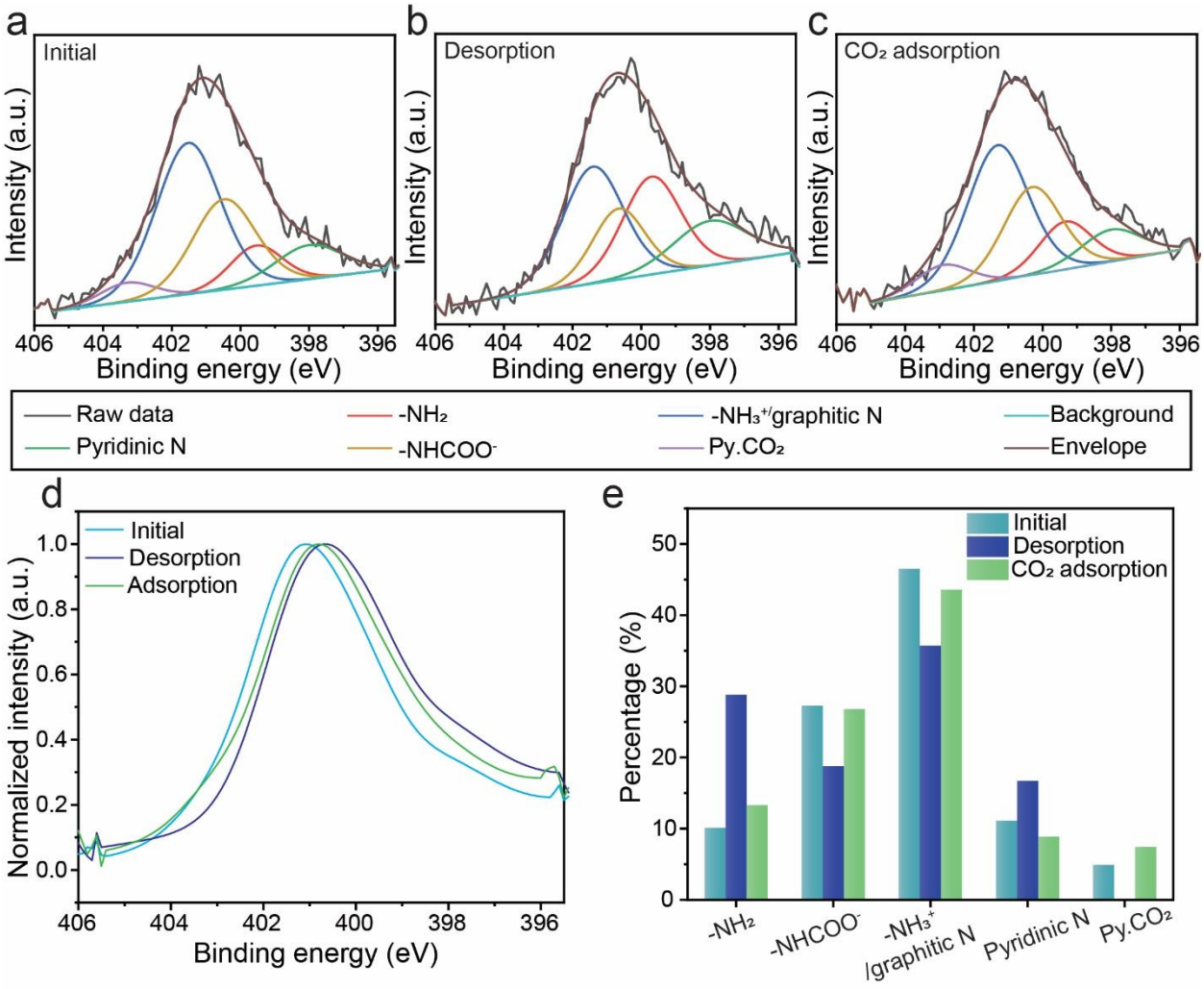

Supplementary Fig. 5. N1s XPS spectra and quantitative analysis of pyridinic-N-substituted graphene. (a) N1s spectrum initial (before desorption), (b) after desorption (150 ºC heating), and (c) after CO_2 adsorption (20 mbar of CO_2 in NAP-XPS), (d) the graph of overlapping the normalized peaks, (e) the quantitative analysis of the three deconvoluted spectra.

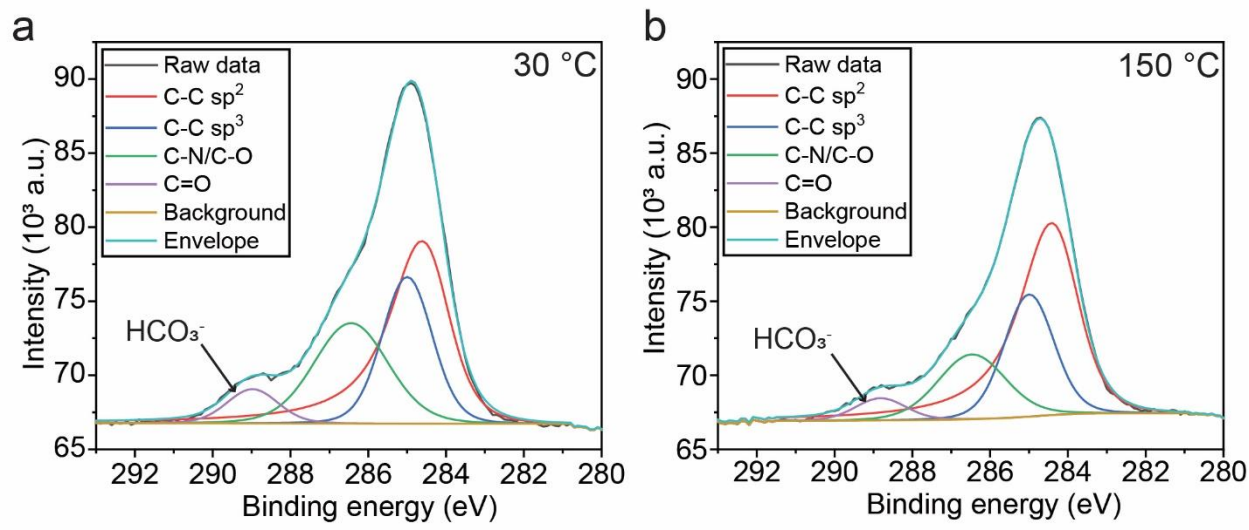

Supplementary Fig. 6. C1s XPS spectra of pyridinic-N-substituted graphene measured at 30 ºC (a) and 150 ºC (b) in XPS UHV chamber.

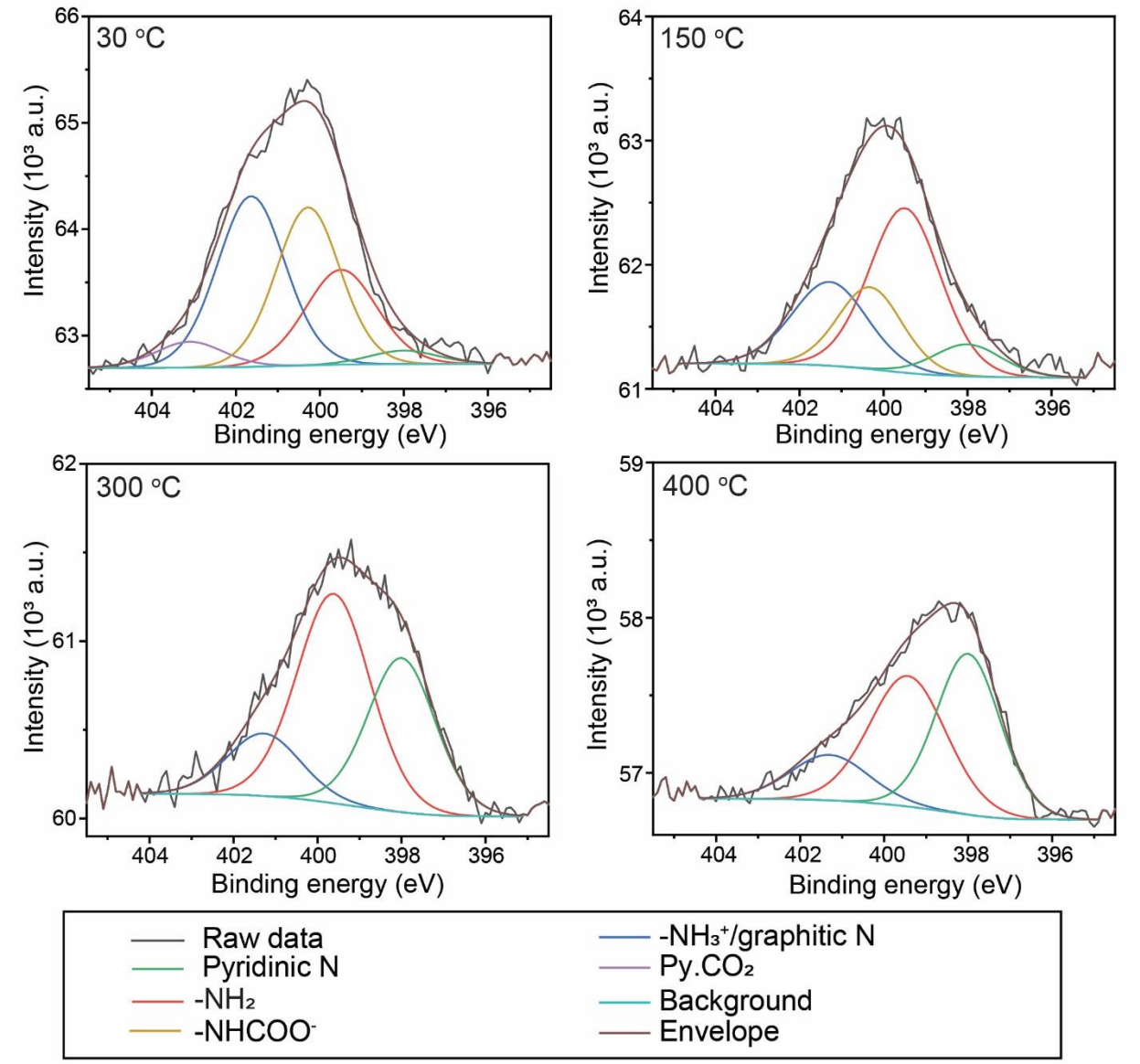

Supplementary Fig. 7. N1s XPS spectra from pyridinic-N-substituted graphene fabricated using 20 °C NH_3 treatment measured at 30, 150, 300, and 400 °C.

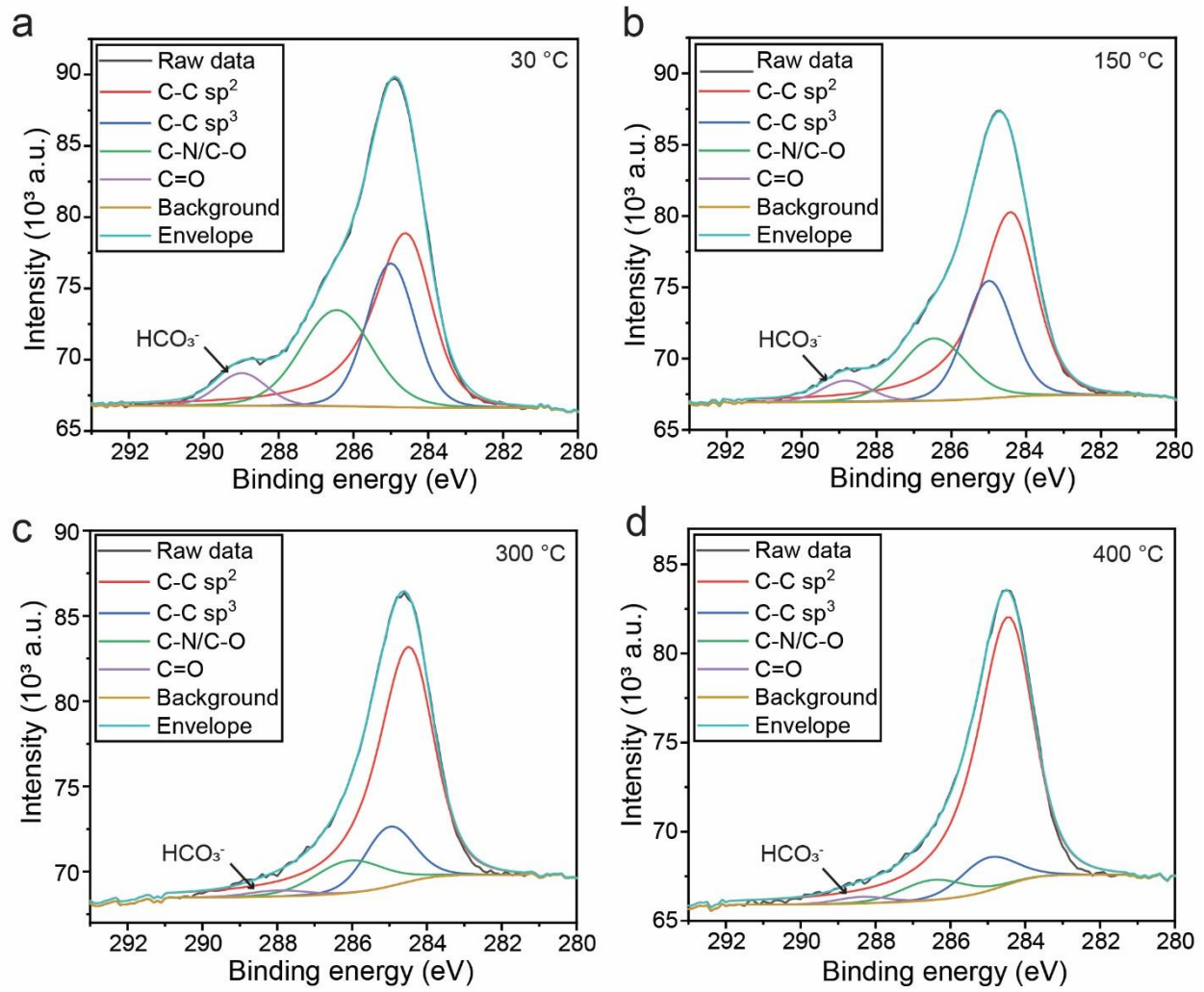

Supplementary Fig. 8. C1s XPS spectra from pyridinic-N-substituted graphene fabricated using 20 °C NH_3 treatment measured at 30, 150, 300, and 400 °C.

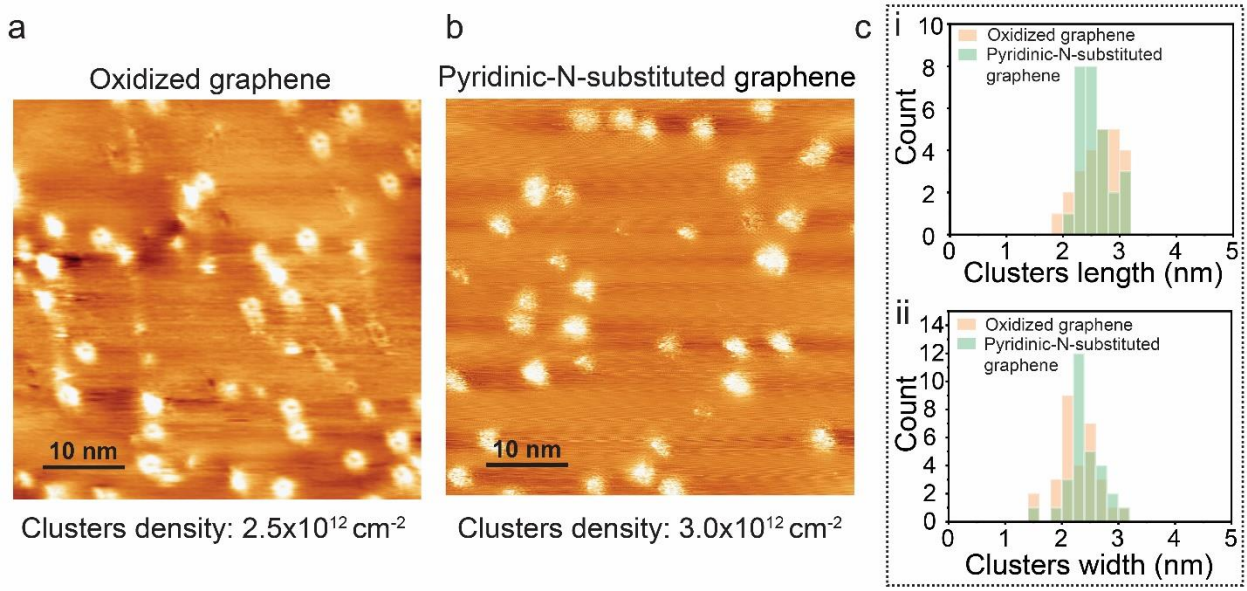

Supplementary Fig. 9. STM images of pyridinic-N-substituted graphene. The STM morphology and the clusters (functional groups on graphene surface) density of oxidized graphene (a) and pyridinic-N-substituted graphene (b). (c) the distribution of the length and width of clusters on oxidized graphene and pyridinic-N-substituted graphene.

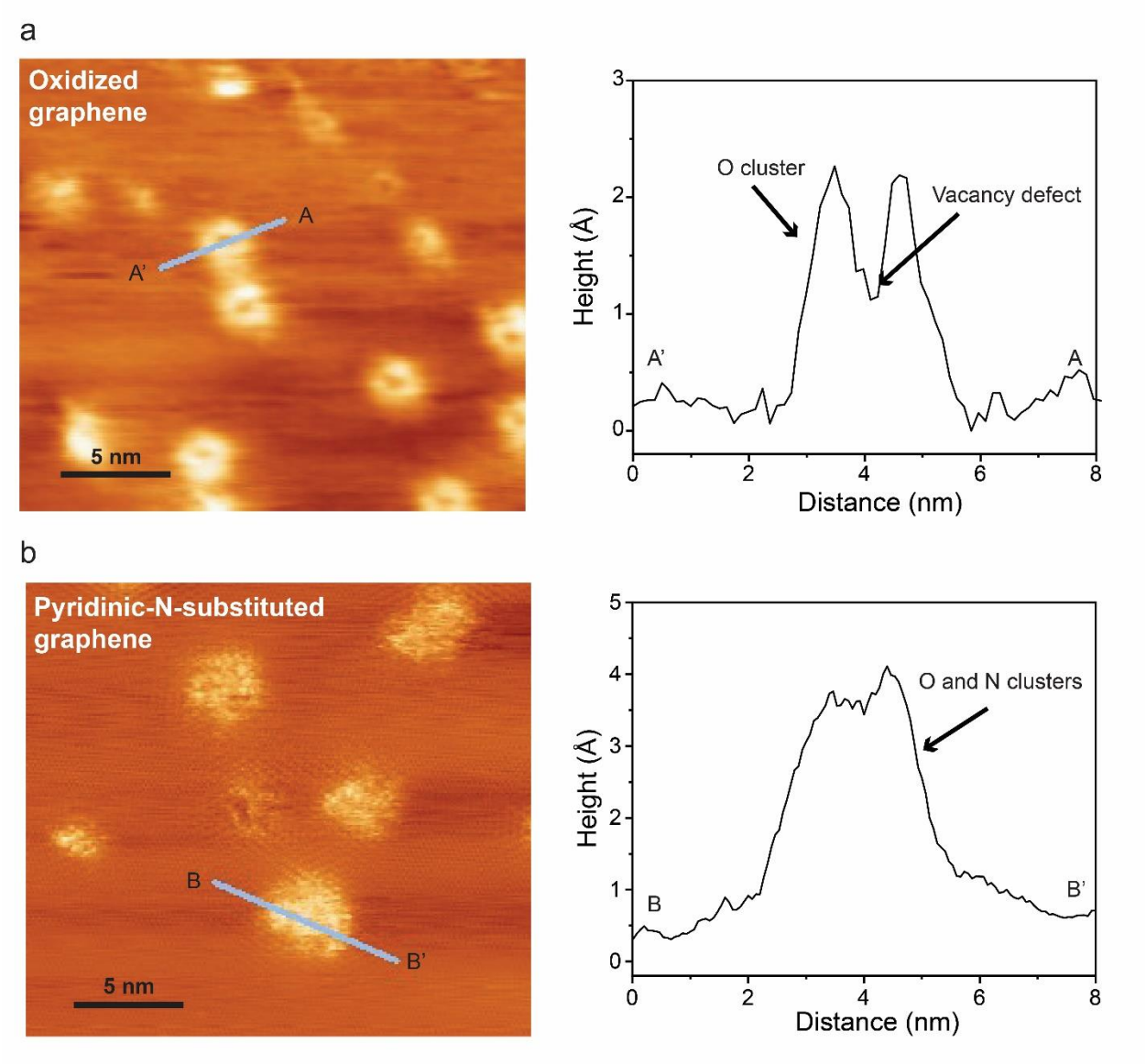

Supplementary Fig. 10. Cross-sectional profile of line A–A' and B–B' drawn in the corresponding STM images of oxidized graphene (a) and pyridinic-N-substituted graphene (b).

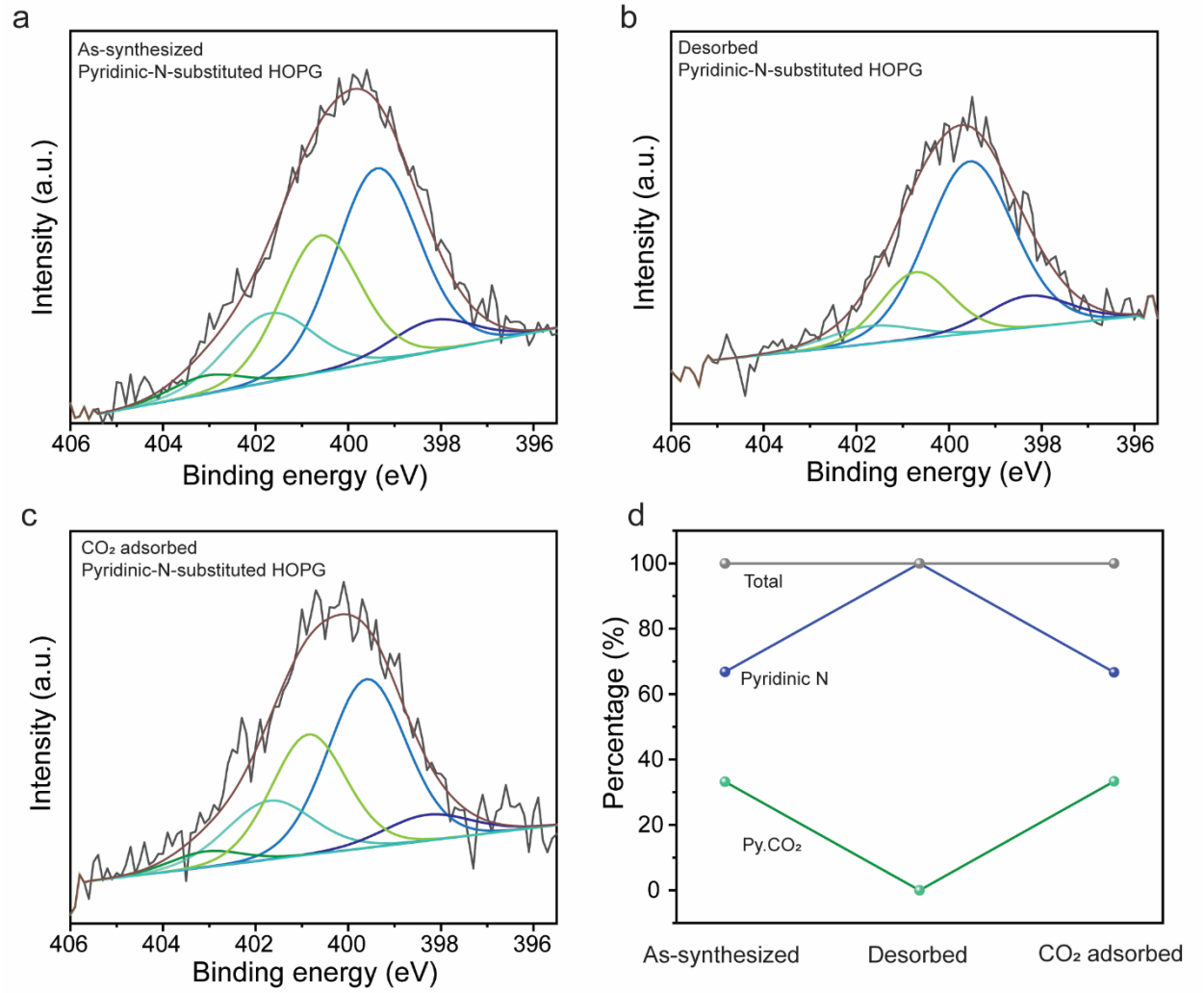

Supplementary Fig. 11. The CO_2 sorption on HOPG treated with O_3 followed by NH_3. N1s XPS spectrum of (a) as-prepared sample, and (b) after 150 ºC heating in the UHV chamber of XPS, and after (c) re-exposure to air for 10 min at 30 ºC. (d) Quantitative analysis of pyridinic-N and Py.CO_2 during CO_2 adsorption and desorption.

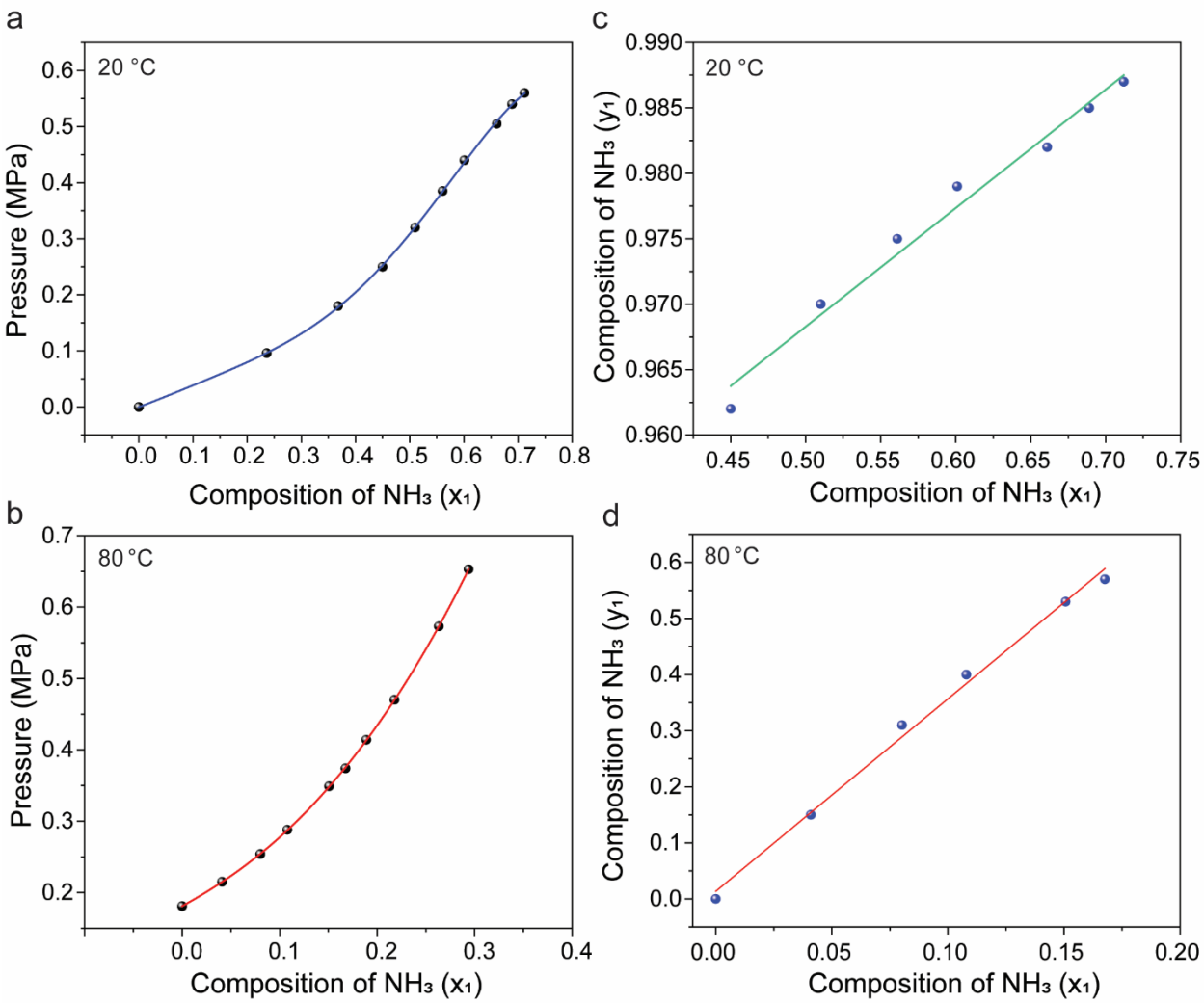

Supplementary Fig. 12. The literature data fitting of NH_3/CH_3OH solution at different temperatures. The non-linear fitting curve of the total pressure of the gas phase (P) versus the NH_3 composition in the liquid phase (x_1) at 20 °C (a) and 80 °C (b) and the linear fitting curve of the molar composition of NH_3 in the vapor phase (y_1) versus the NH_3 composition in liquid phase (x_1) at 20 °C (c) and 80 °C (d).

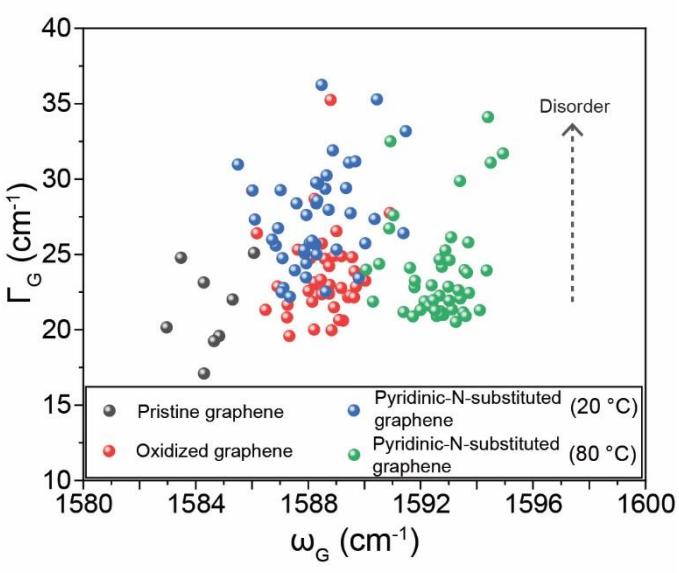

Supplementary Fig. 13. Scatter plots of *G* peak full-width at half-maximum (FWHM, Γ_G) versus *G* peak position (ω_G) data points adapted from pristine, oxidized graphene, pyridinic-N-substituted graphene treated with 20 and 80 °C NH_3 treatment.

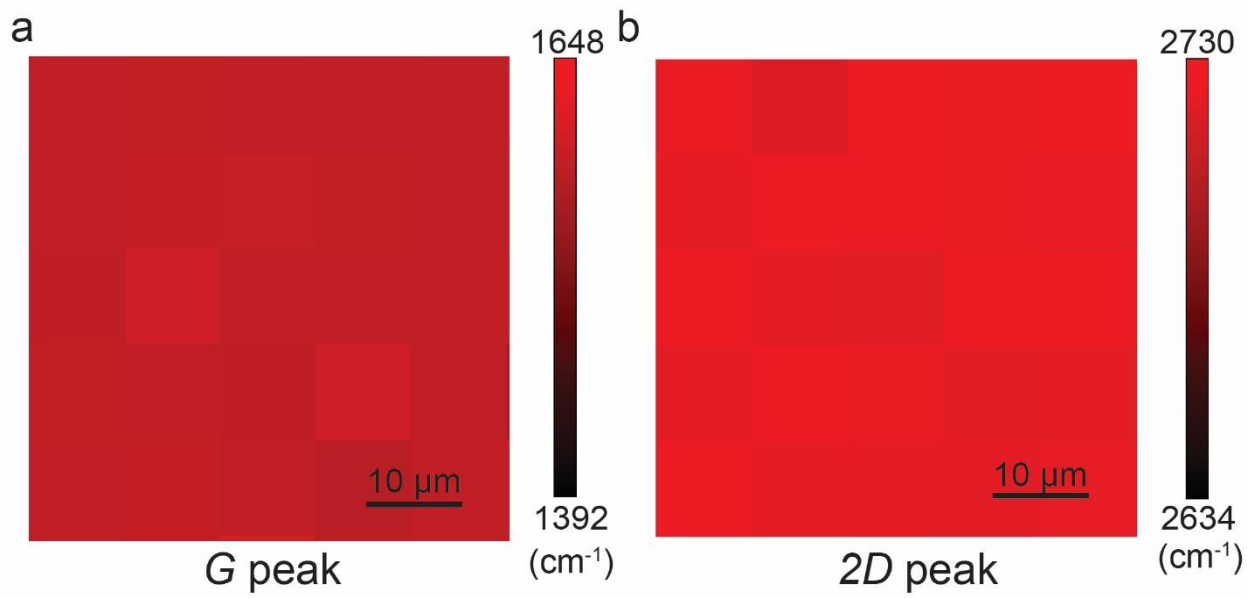

Supplementary Fig. 14. Raman mapping of *G* peak shift (a) and *2D* peak shift (b) data points of pyridinic-N-substituted graphene fabricated using 20 ^{o}C NH_3 treatment.

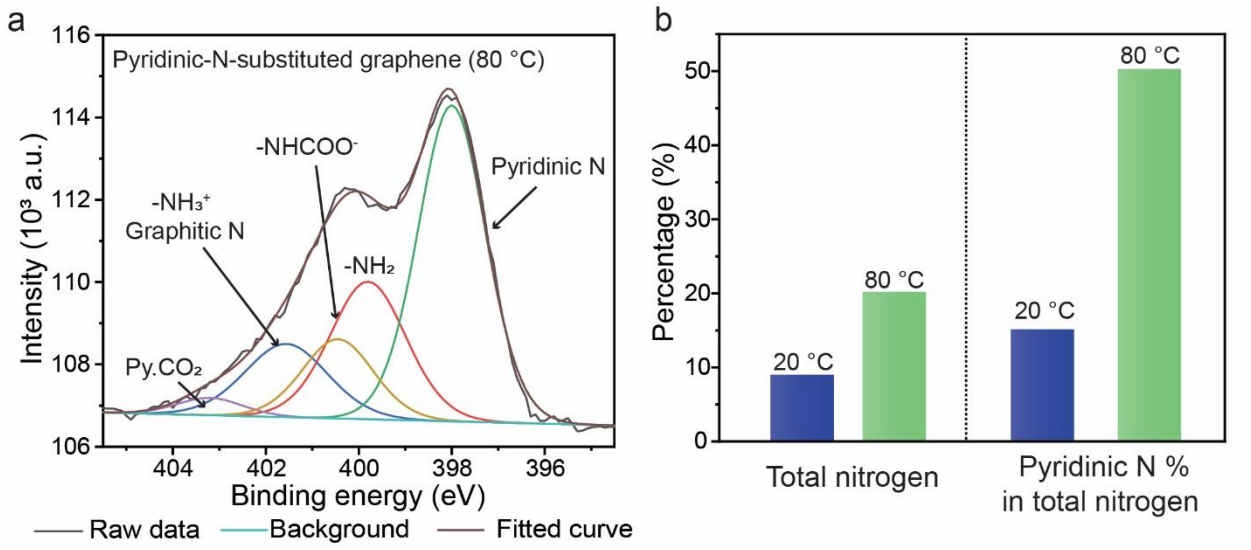

Supplementary Fig. 15. (a) XPS spectrum of pyridinic-N-substituted graphene treated at 80 ºC and (b) the quantification analysis of total N percentage and pyridinic N percentage in the total amount of nitrogen.

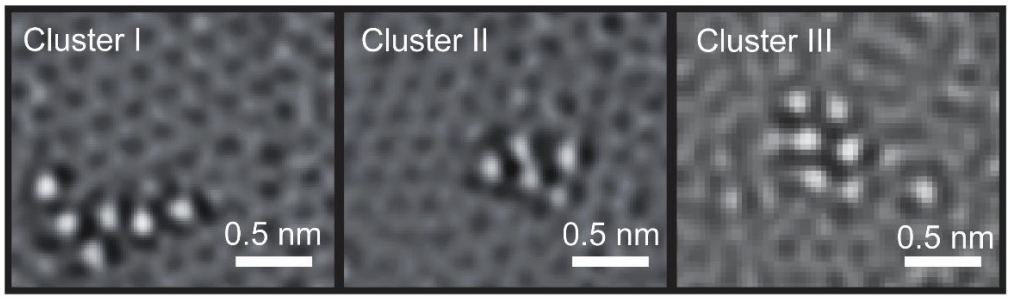

Supplementary Fig. 16. The AC-HRTEM images showing the bright clusters on the pyridinic-N-substituted graphene 2D pores.

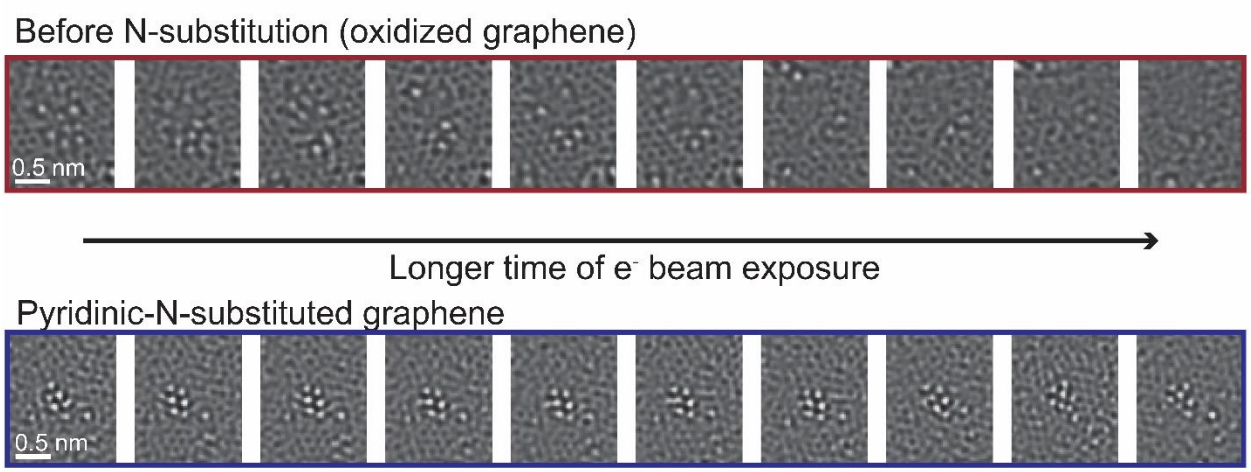

Supplementary Fig. 17. The evolution of clusters on oxidized graphene (O-cluster) and pyridinic-N-substituted graphene (N-cluster) under electron beam in AC-HRTEM (electron dose of 4.7×10^5 e^- $Å^{-2}$), showing that N-clusters on pyridinic-N-substituted graphene are more stable under the electron beam.

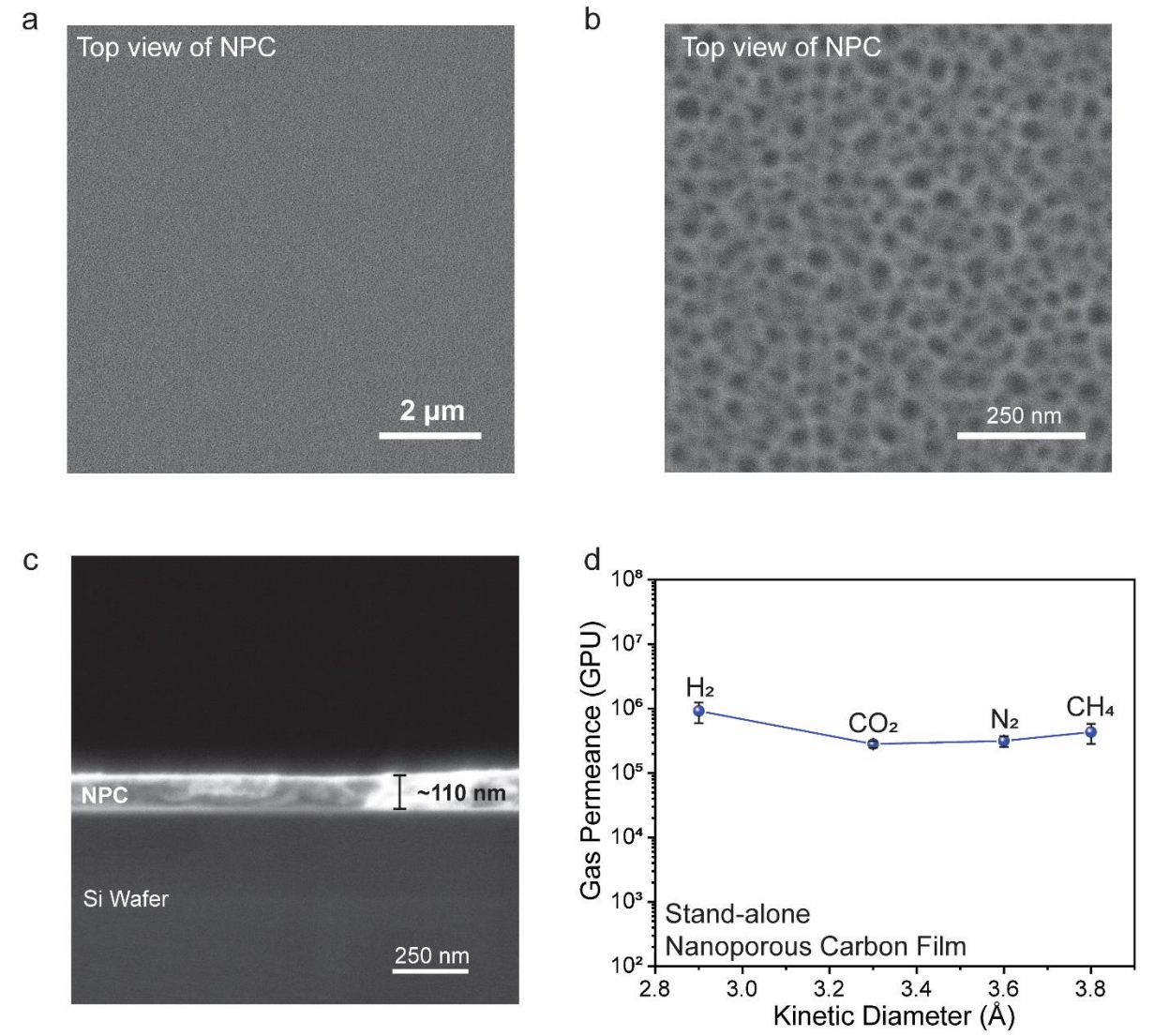

Supplementary Fig. 18. SEM characterization and gas measurement of the stand-alone NPC film. SEM images of the surface of NPC film in (a) lower magnitude and (b) high magnitude. (c) SEM image of the cross-section of NPC film deposited on a silicon wafer. (d) Single gas permeation results of NPC membranes. All the gas measurements were conducted at 30 °C and 2 bar feed pressure. The error bars refer to the standard deviation in the separation factor and permeance across three membranes. The center of each error bar represents the average separation factor and permeance calculated from the NPC membranes.

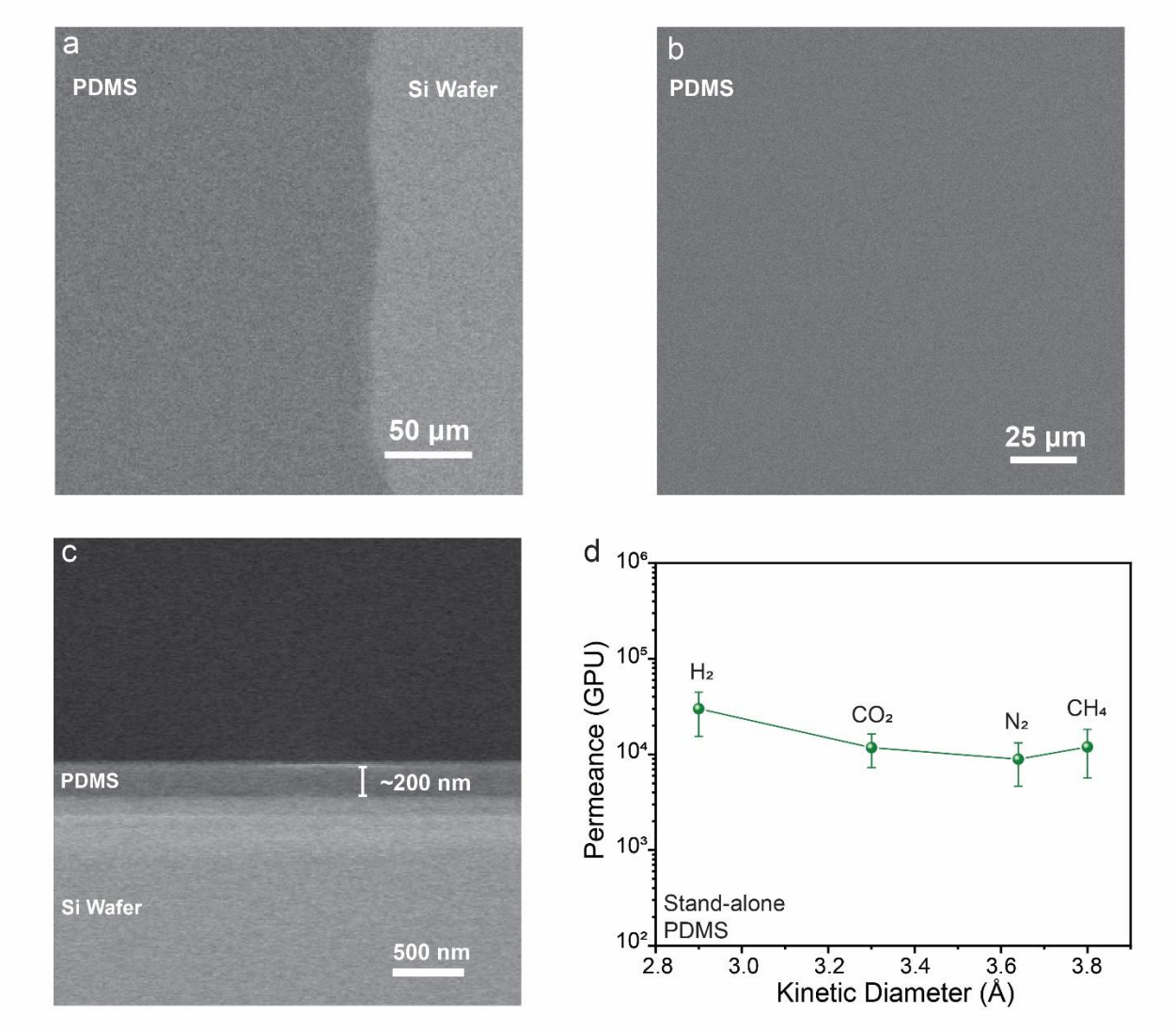

Supplementary Fig. 19. SEM characterization and gas measurement of the stand-alone PDMS film. SEM images of the surface of PDMS film deposited on silicon wafer in (a) lower magnitude and (b) high magnitude. (c) SEM image of the cross-section of PDMS film deposited on a silicon wafer. (d) Single gas permeation results of PDMS membranes. All the gas measurements were conducted at 30 °C and 2 bar feed pressure. The error bars refer to the standard deviation in the separation factor and permeance across four membranes. The center of each error bar represents the average separation factor and permeance calculated from the PDMS membranes.

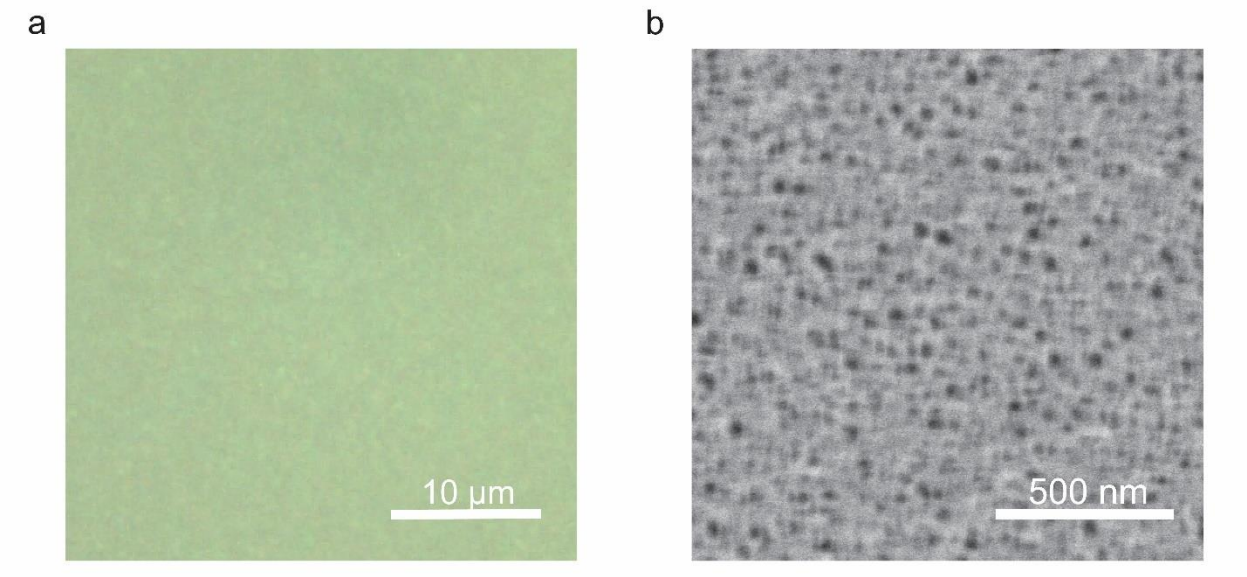

Supplementary Fig. 20. (a) The optical image and (b) SEM image of the porous polymeric support (PBI) used to fabricate centimeter-scale membrane, revealing a smooth surface hosting ~20 nm pores.

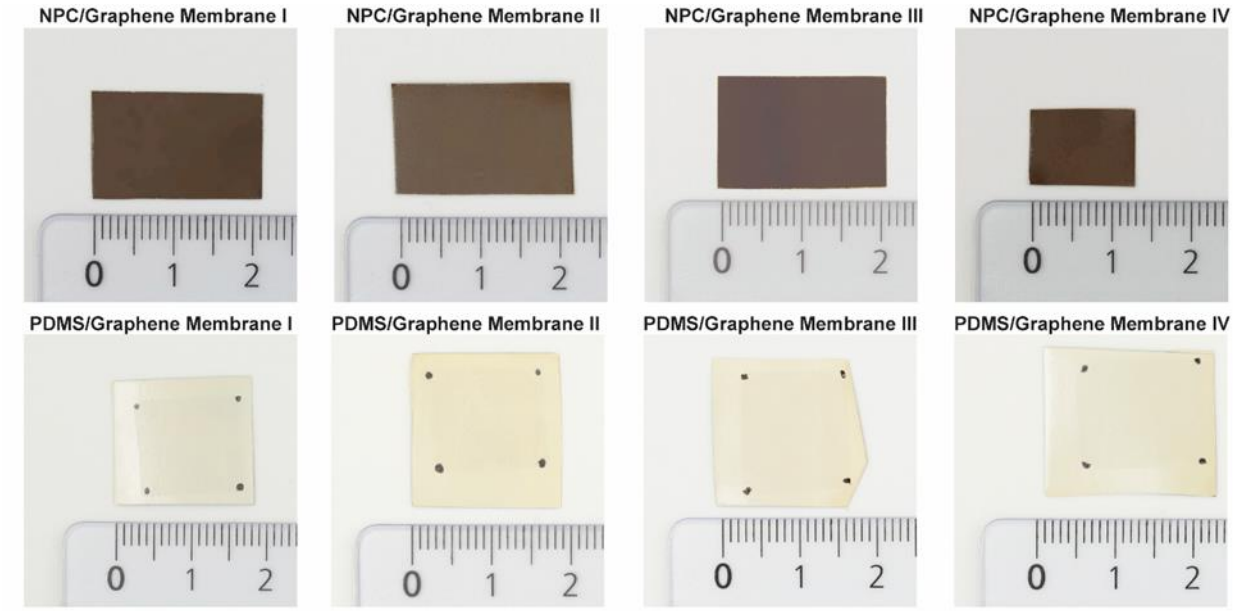

Supplementary Fig. 21. Pictures of pyridinic-N-substituted graphene prepared by different support films (NPC and PDMS). The edges of support of NPC/graphene membranes were cut. The edges of the PDMS/graphene film on polymeric support are highlighted in black dots.

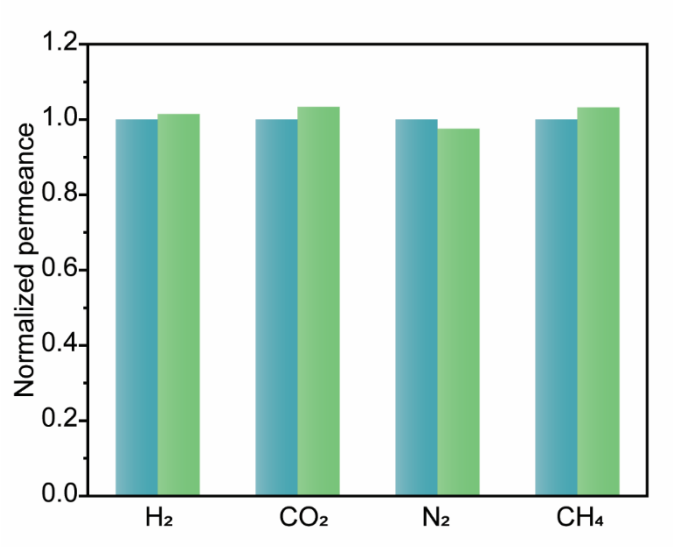

Supplementary Fig. 22. Single gas measurement result of stand-alone NPC support film before and after NH_3 treatment at 20 ºC. All the gas measurements were conducted at 30 ºC and 2 bar feed pressure.

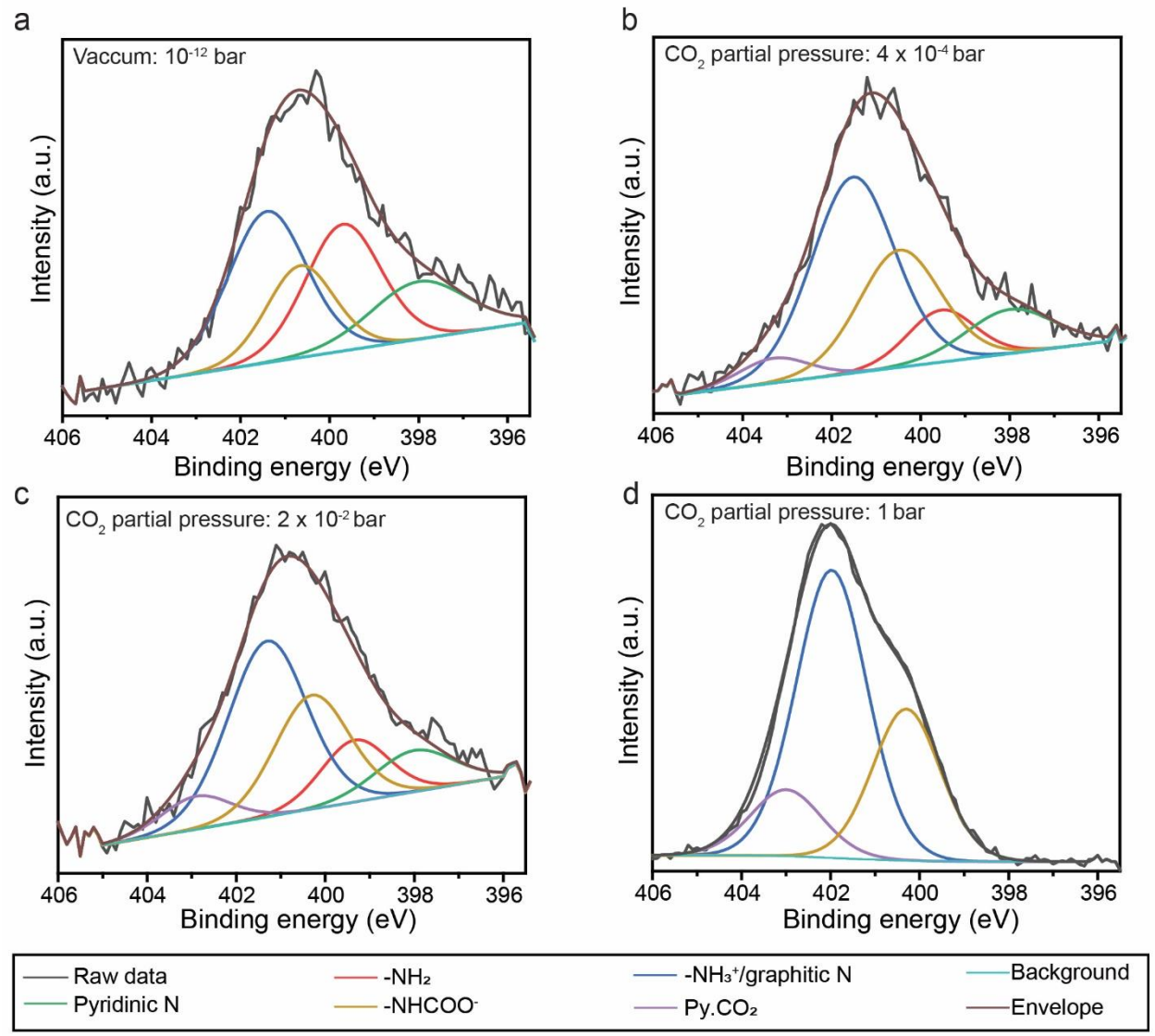

Supplementary Fig. 23. XPS N1s spectrum of pyridinic-N-substituted graphene measured under different CO_2 partial pressure (10^{-12}, 4×10^{-4}, 2×10^{-2}, and 1 bar), showing the different extent of CO_2 adsorption on the N functional groups.

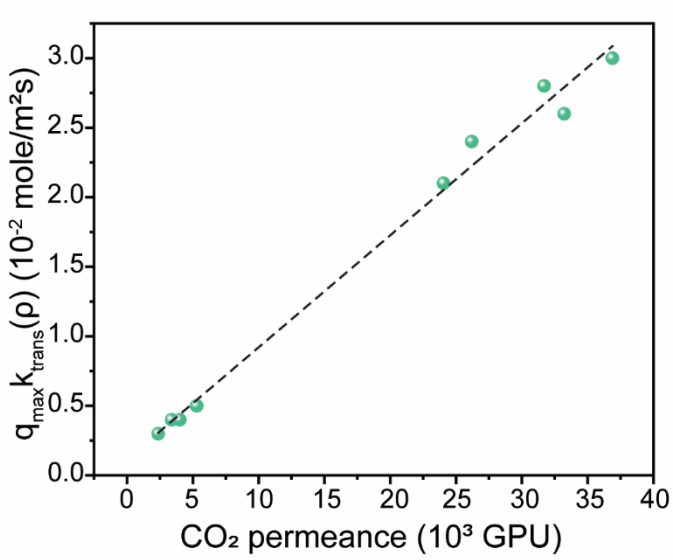

Supplementary Fig. 24. The curve fitting of $q_{max}k_{trans}(\rho)$ versus the CO_2 permeance measured at 12 mbar. The data were calculated and measured based on pyridinic-N-substituted graphene/NPC membranes. Here, q_{max} corresponds to the maximum number of CO_2 molecules that can adsorb under a given temperature and pressure. $k_{trans}(\rho)$ is the translocation coefficient (effective rate per gas molecule) for gas molecules passing through pores. ρ is the pore density.

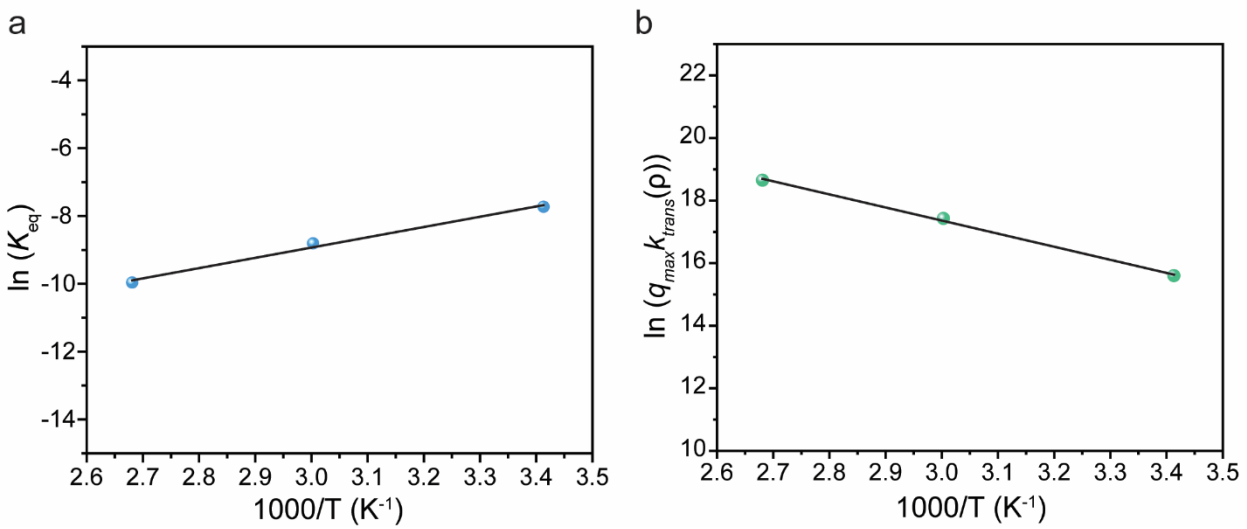

Supplementary Fig. 25. (a) The linear fitting plot of ln(K_{eq}) versus the reciprocal measurement temperature for adsorption energy. (b) The linear fitting plot of ln($q_{max}k_{trans}(\rho)$) versus the reciprocal measurement temperature for activation energy.

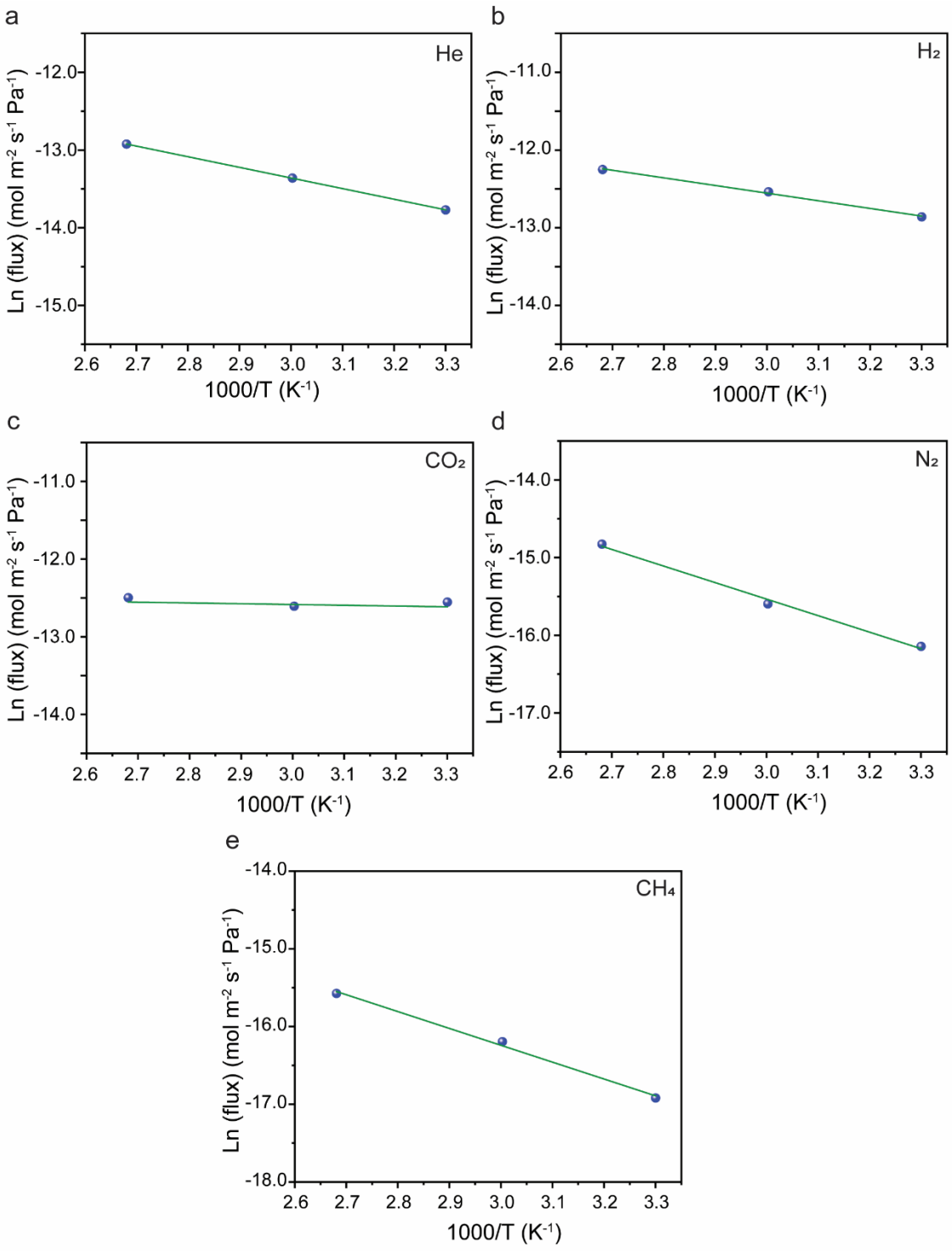

Supplementary Fig. 26. A linear fitting plot of the single gas permeation versus reciprocal measurement temperature for apparent activation energy. The data were calculated and measured based on pyridinic-N-substituted graphene/NPC membranes.

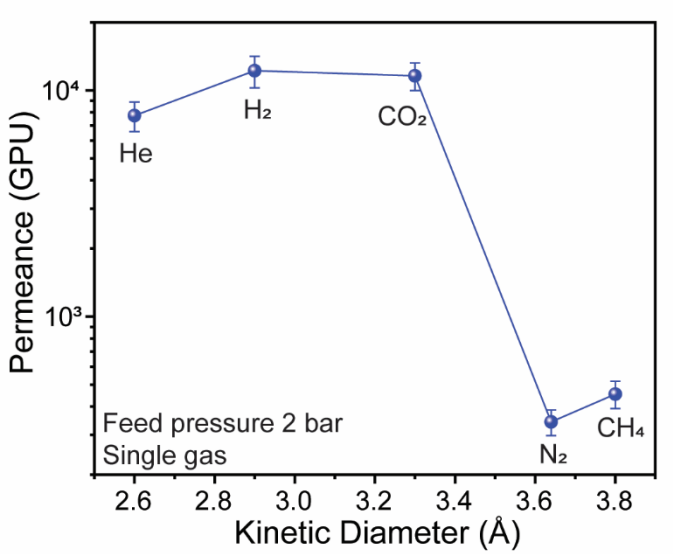

Supplementary Fig. 27. Single-gas permeation results of pyridinic-N-substituted graphene/NPC membranes measured at 30 ºC, 2 bar. The error bars refer to the standard deviation in the separation factor and permeance across three membranes. The center of each error bar represents the average separation factor and permeance calculated from the pyridinic-N-substituted graphene/NPC membranes.

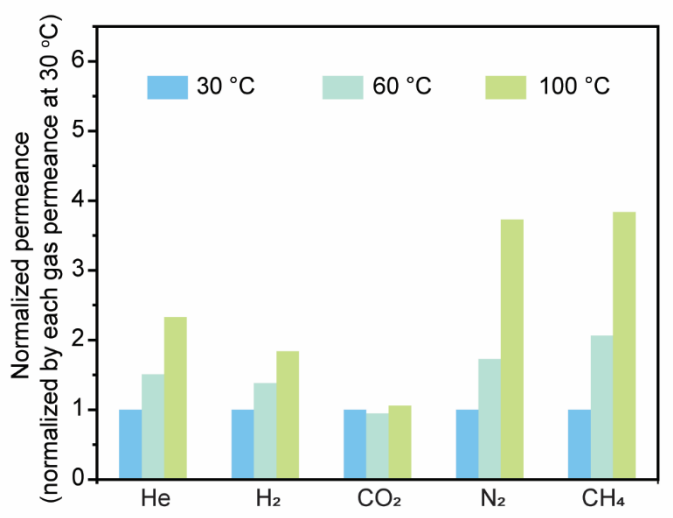

Supplementary Fig. 28. Normalized single-gas permeation results of pyridinic-N-substituted graphene/NPC membranes measured at 30, 60, and 100 ºC (each gas permeance is normalized by the same gas permeance at 30 ºC).

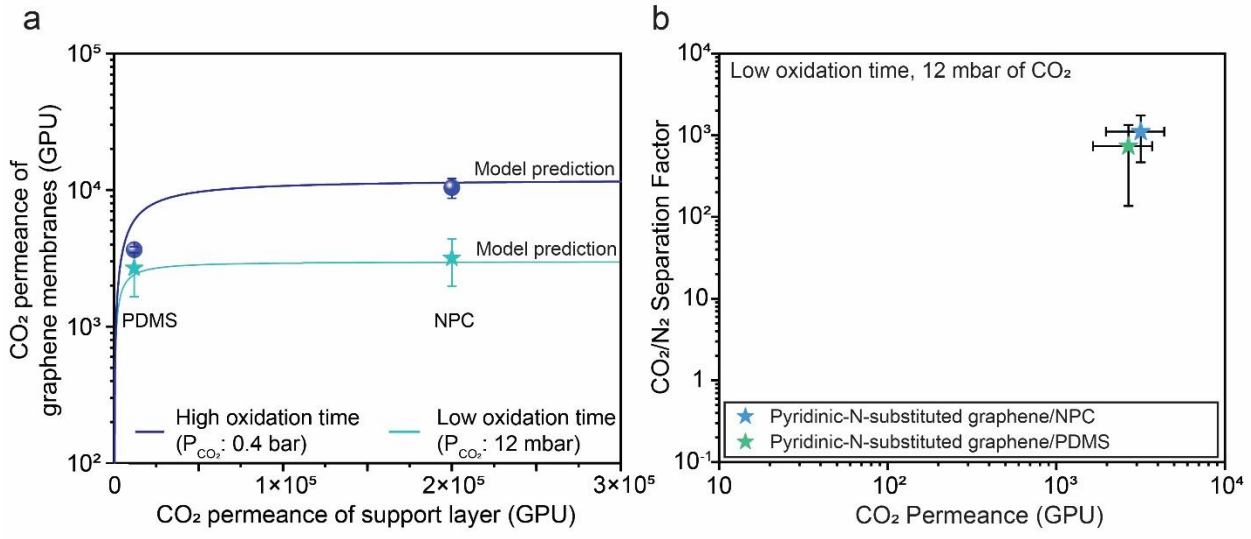

Supplementary Fig. 29. Comparison of CO_2 permeance and CO_2/N_2 separation performance of pyridinic-N-substituted graphene membrane prepared by three different support films (NPC and PDMS), showing porous graphene controlling gas transport. (a) The evolution of CO_2 permeance of graphene membranes (y-axis) as the function of CO_2 permeance of support film (x-axis). Circles (stars) represent graphene membranes prepared by high (low) oxidation time at 0.4 bar (12 mbar) of CO_2 partial pressure at the feed. The blue and cyan lines are the predictions from the gas transport resistance model[27] for graphene prepared by high and low oxidation time, respectively. The model shows that the transport resistance of the support layer yielding high permeance does not contribute to graphene membranes. The error bars refer to the standard deviation in the separation factor and permeance across several membranes. The center of each error bar represents the average separation factor and permeance calculated from the graphene membranes. For graphene membranes etched with high oxidation times, there were six and three samples each for graphene/NPC and graphene/PDMS. For membranes etched with low oxidation times, there were ten samples of graphene/NPC and four samples of graphene/PDMS. (b) Agreement between CO_2/N_2 separation performance of pyridinic-N-substituted graphene membrane prepared using low oxidation time with all two support films. The measurement was carried out under dilute CO_2 conditions (12 mbar) at 30 °C.

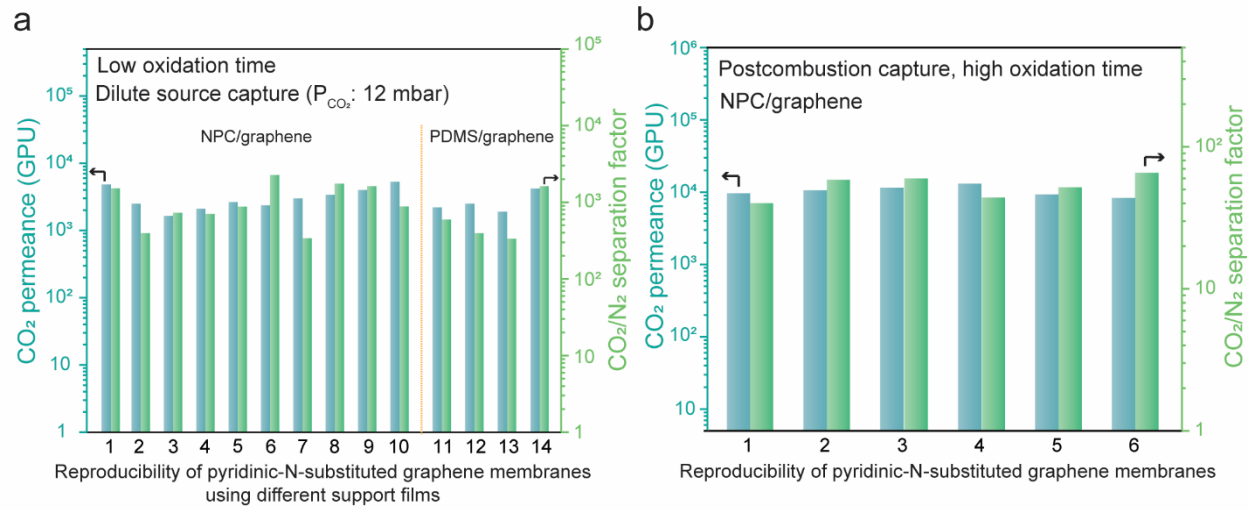

Supplementary Fig. 30. Reproducibility of pyridinic-N-substituted graphene membranes supported by two different support layers (NPC and PDMS).

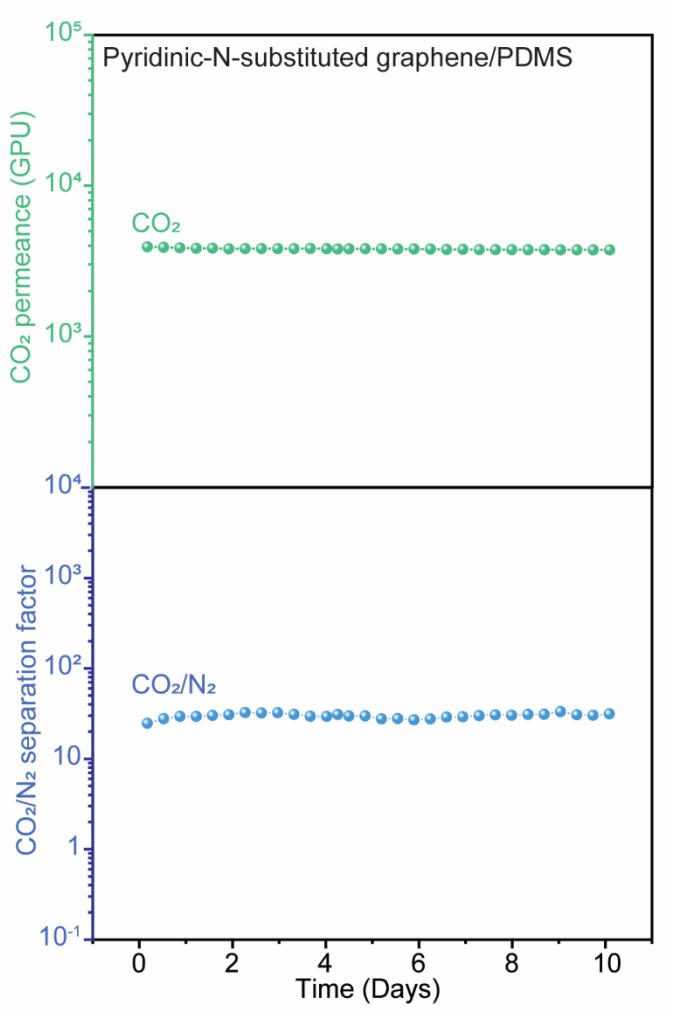

Supplementary Fig. 31. The stability test of pyridinic-N-substituted graphene/PDMS membrane measured under 20% CO_2/N_2 mixed gas at 30 °C. The graphene was etched with a high oxidation time (60 min).

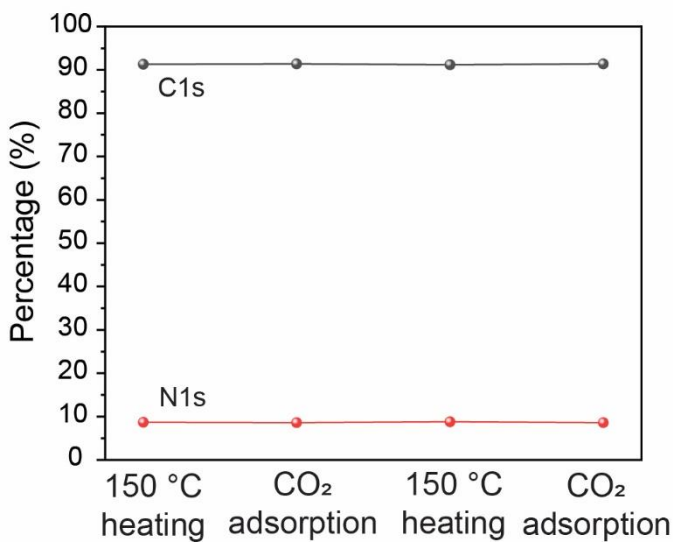

Supplementary Fig. 32. Quantification analysis of C and N percentage after 150 ºC heating under vacuum and 20 mbar CO_2 at 30 ºC.

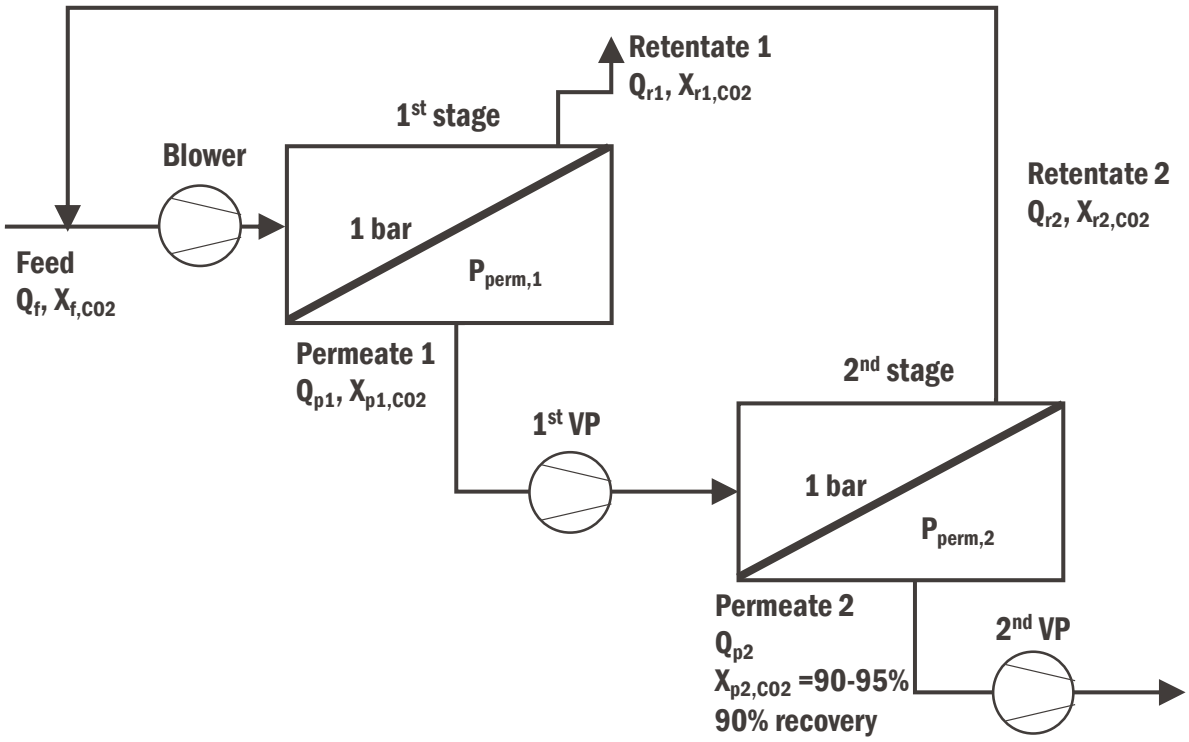

Supplementary Fig. 33. Representation of the double-stage membrane process with permeate under vacuum and recycle of the 2nd retentate, used for CO_2 capture from concentrated feeds.

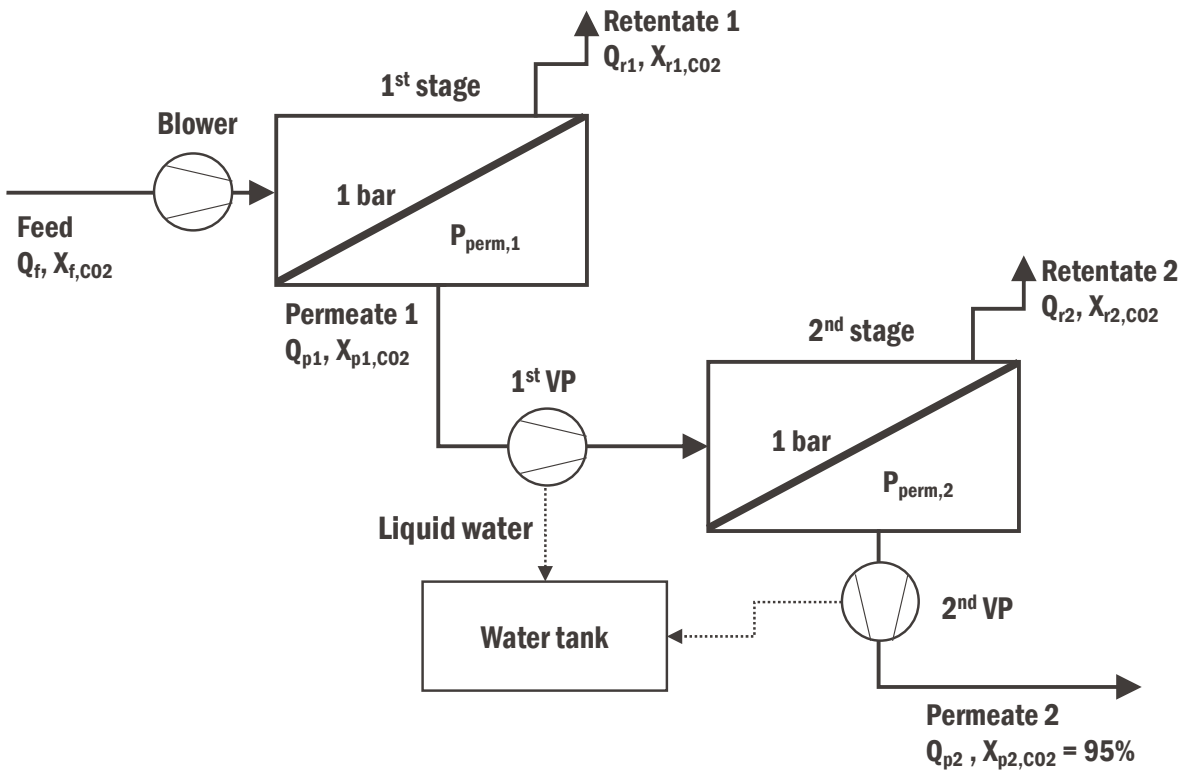

Supplementary Fig. 34. Representation of the double-stage membrane process with permeate under vacuum and intermediate water condensation, used for CO_2 capture from low-concentration feeds.

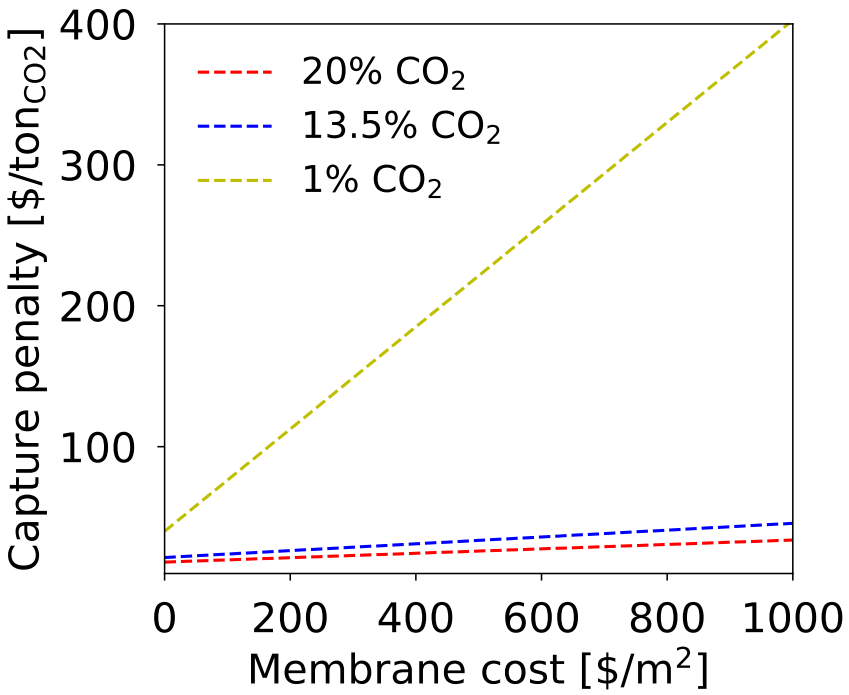

Supplementary Fig. 35. Sensitivity analysis with variable specific membrane cost for three CO_2 inlet feed concentrations.

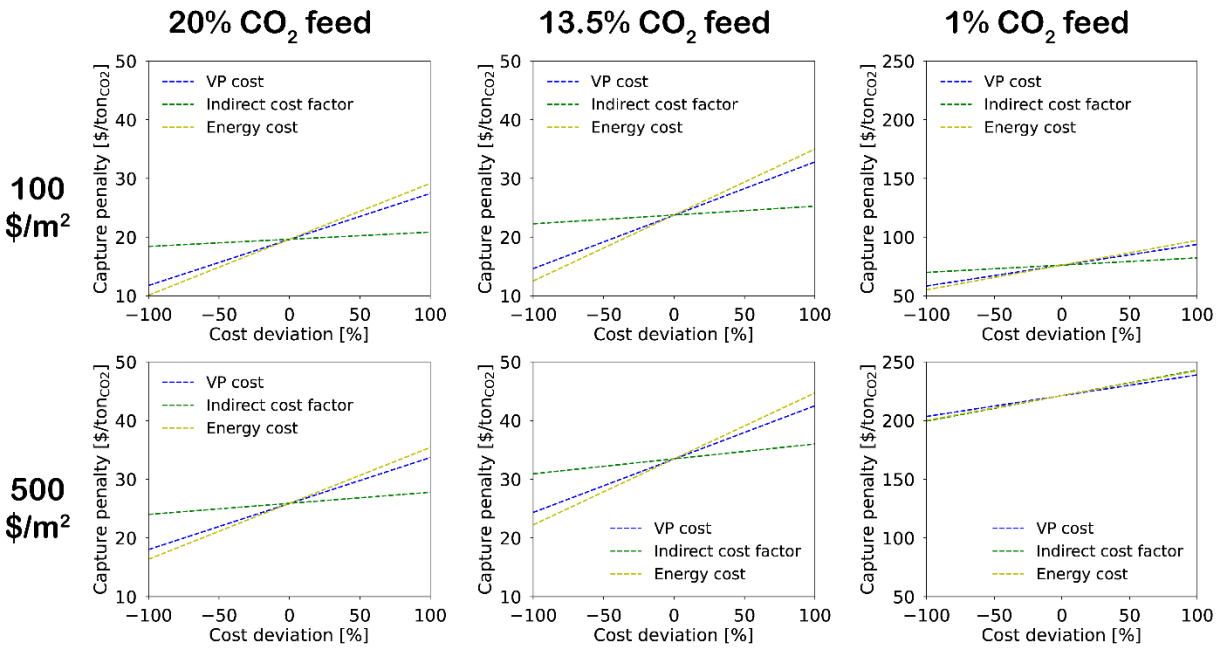

Supplementary Fig. 36. Sensitivity analysis with variable specific vacuum pump cost, indirect cost factor and specific energy cost for three CO_2 inlet feed concentrations and with two given values of specific membrane cost (upper charts: 100 $/m^2, lower charts: 500 $/m^2).

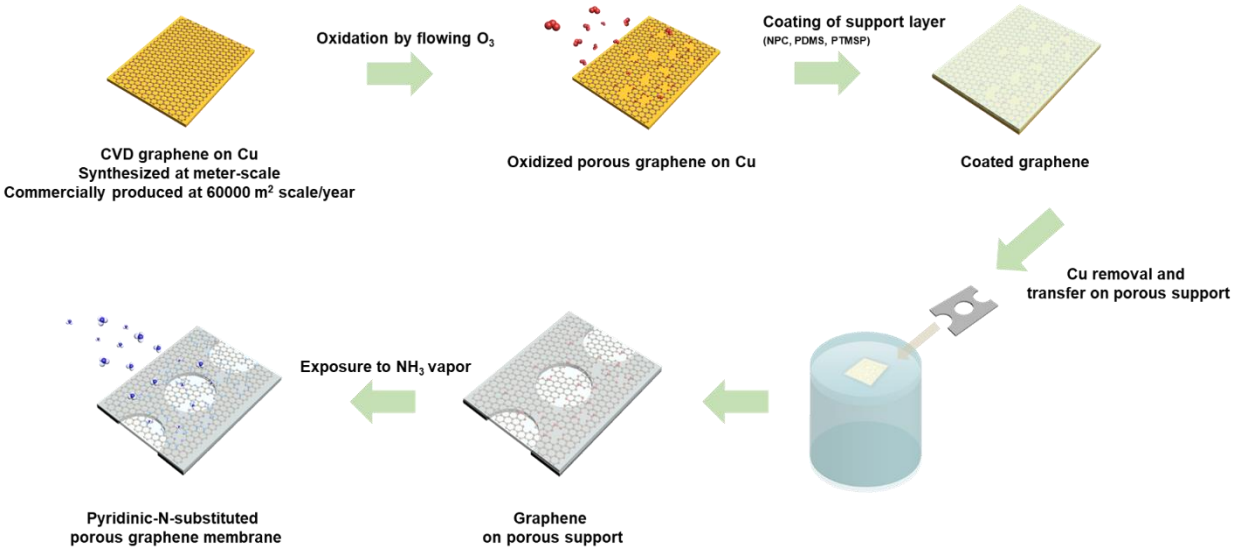

Supplementary Fig. 37. Schematic of the fabrication procedure for pyridinic-N-substituted graphene membranes.

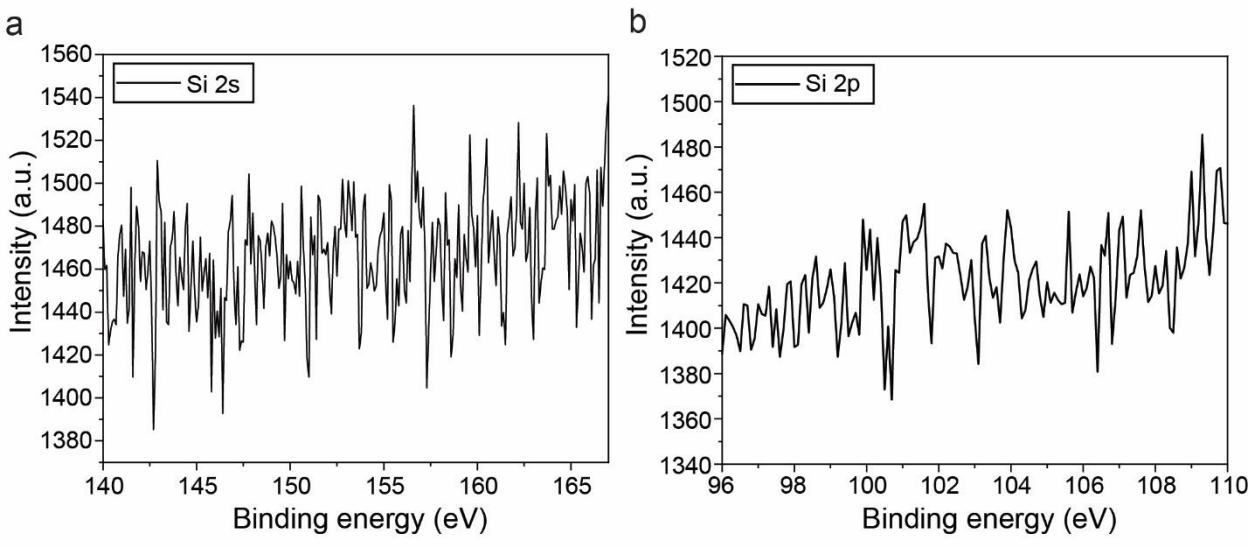

Supplementary Fig. 38. Si2s and Si2p XPS spectra of pyridinic-N-substituted graphene showing the lack of Si signal indicating that the mechanically reinforcing layer of PTMSP was successfully removed for the XPS analysis.

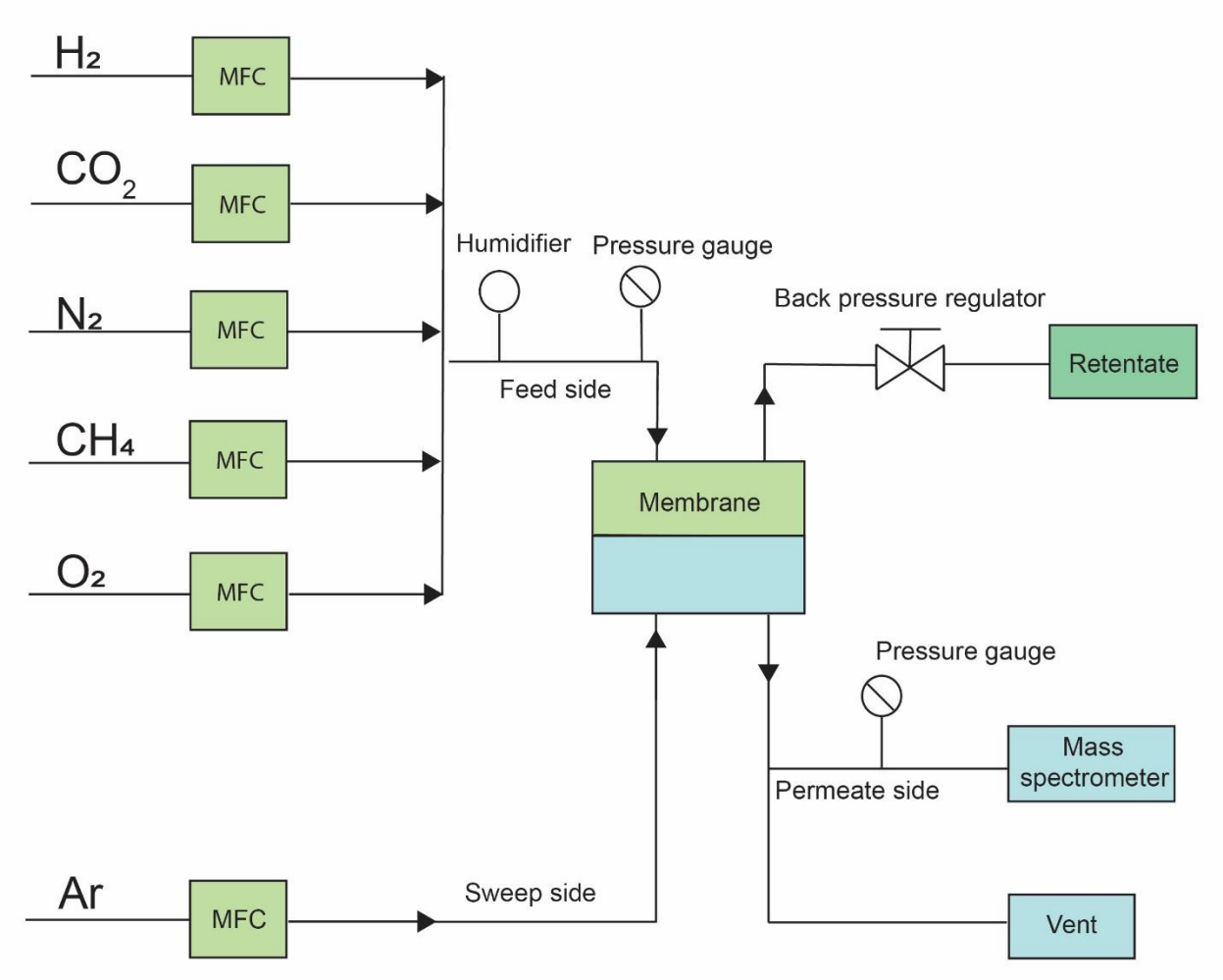

Supplementary Fig. 39. Schematic of the gas permeation setup.

Supplementary Table 1-13

Supplementary Table 1. The evolution of N-functional groups percentage during two-cycle desorption and CO_2 adsorption in NAP-XPS chamber. The desorption was conducted by 150 ^oC heating, and the adsorption was conducted under 20 mbar CO_2 partial pressure in NAP-XPS.

	-NH_2 (%)	-$NHCOO^-$ (%)	NH_3^+ /graphitic N (%)	pyridinic N (%)	Py.CO_2 (%)
Initial	10.1	27.3	46.5	11.1	4.9
1st desorption	28.8	18.8	35.7	16.7	0.0
1st CO_2 adsorption	13.3	26.8	43.6	8.9	7.4
2nd desorption	29.0	18.9	35.5	16.6	0
2nd CO_2 adsorption	13.8	26.9	43.5	8.5	7.4

Supplementary Table 2. The evolution of N-functional groups percentage as the function of temperature. The sample was loaded into XPS chamber directly after NH_3-treatment. The percentage of N-functional groups was extracted from N1s spectrum, and the percentage of C=O was extracted from C1s spectrum.

T (^oC)	-NH_2 (%)	-$NHCOO^-$ (%)	NH_3^+ /graphitic N (%)	Pyridinic N (%)	Py.CO_2 (%)	C=O (%) (HCO_3^- & semiquinone)
150	39.0	21.8	25.8	13.3	0	4.4
300	50.6	0.0	15.0	34.4	0	1.7
400	41.8	0.0	14.9	43.3	0	1.6

Supplementary Table 3. The estimated change of Fermi level and electron-carrier density of graphene samples based on *G* peak shift adapted from the Raman spectrum.

	ω_G (cm^{-1})	ΔE_F (meV)
Pristine Graphene	1584	-
Oxidized Graphene	1588	-155.6
Pyridinic-N-substituted Graphene (20 ºC)	1588	-155.6
Pyridinic-N-substituted Graphene (80 ºC)	1592	-226.0

Supplementary Table 4. Mixed gas permeation results for pyridinic-N-substituted graphene/NPC membranes treated with different NH_3 reaction times at 20 ºC (CO_2 concentration of 20 mol%, T = 30 ºC, feed pressure = 2 bar). The graphene was etched with a high oxidation time (60 min).

Condition	CO_2 Permeance (GPU)	CO_2/N_2 SF
Before N-substitution	47030±5780	13.7±3.0
After 1.5h N-substitution	13320±900	27.7±3.2
After 24h N-substitution	10420±1710	53.3±9.8

Supplementary Table 5. The percentage of $Py.CO_2$ in the total nitrogen functional groups and the coverage of adsorbed CO_2 on pyridinic N.

CO_2 partial pressure (bar)	The percentage of $Py.CO_2$ in the total N	The coverage of adsorbed CO_2 on pyridinic N (%)
10^{-12}	0	0
4×10^{-4}	4.9	30
2×10^{-2}	7.4	45
1	12.8	100

Supplementary Table 6. Mixed gas permeation results for pyridinic-N-substituted graphene/NPC membrane. Graphene was etched with low oxidation time (30 min). (CO_2 concentration of 0.6, 1.0, 2.0, 7.0, 10.0, 15.0, 20.0, 50.0 mol%, feed pressure = 2 bar, T = 30 °C).

%	0.6	1.0	2.0	7.0	10.0	15.0	20.0	50.0
(bar)	(0.012)	(0.02)	(0.04)	(0.14)	(0.2)	(0.3)	(0.4)	(1.0)
CO_2 permeance (GPU)	5300	4400	2910	2630	1560	1530	1460	1310
CO_2/N_2 SF	881	719	460	394	234	216	230	206

Supplementary Table 7. Mixed gas permeation results for pyridinic-N-substituted graphene/NPC membranes. The graphene was etched with a high oxidation time (60 min). (CO_2 concentration of 0.6%, feed pressure = 1.4 bar, T = 30 ºC).

Membrane	CO_2 Permeance (GPU)	CO_2/N_2 SF
Pyridinic-N-substituted graphene/NPC membranes	33880 ± 8085	150 ± 64

Supplementary Table 8. Mixed gas permeation results for pyridinic-N-substituted graphene/NPC membranes. The graphene was etched with low oxidation time (30 min). (CO_2 concentration of 0.6%, feed pressure = 1.4 bar, T = 30 ºC).

Membrane	CO_2 Permeance (GPU)	CO_2/N_2 SF
Pyridinic-N-substituted graphene/NPC membranes	3770 ± 1239	1428 ± 911

Supplementary Table 9. Mixed gas permeation results for centimeter-scale pyridinic-N-substituted graphene/NPC membrane (T = 30 °C). Graphene was etched with low oxidation time (30 min).

CO_2 partial pressure (mbar)	CO_2 Permeance (GPU)	CO_2/N_2 SF
12	4830	1515
8.4	5900	2585

Supplementary Table 10. Mixed gas permeation results of pyridinic-N-substituted graphene/NPC membranes measured under different CO_2 partial pressure environments. (T = 30 °C), and the estimated fraction of size-sieving pyridinic-N-substituted pores, C_{py}, and the maximum CO_2 loading translocating through pyridinic-N-substituted pores via the size-sieving pathway. (The CO_2 permeance was measured at 20 vol% of CO_2/N_2 mixture with 2 bar feed pressure).

		CO_2 Permeance (GPU)							C_{py}	$q_{max}k_{trans}(\rho)$ (mole/m^{2}s)
%		0.6	1.0	2.0	3.5	10.0	15.0	20.0		
(bar)		(0.012)	(0.02)	(0.04)	(0.07)	(0.2)	(0.3)	(0.4)		
Low Oxidation (30 mins)	M1	2370	1650	980	740	270	230	250	1	0.003
	M2	3390	2130	1150	870	700	680	720	0.999	0.004
	M3	4010	3120	2520	1680	880	860	840	0.998	0.004
	M4	5300	4400	2910	2630	1560	1530	1460	0.995	0.005
High Oxidation (60 mins)	M5	24060	19600	16200	14300	9140	8850	8350	0.964	0.021
	M6	26200	21400	17650	15580	9360	9210	9300	0.962	0.024
	M7	31700	25700	21450	19200	11060	10770	10570	0.954	0.028
	M8	33230	25540	21860	20540	12770	12990	11570	0.948	0.026
	M9	36890	27300	22180	20210	12850	12900	13080	0.943	0.030

Supplementary Table 11. Normalized CO_2 permeance (normalized by the CO_2 permeance at 400 mabr) from a low porosity pyridinic-N-substituted graphene/NPC membrane measured under different temperatures and CO_2 partial pressure environment with a total feed pressure of 2 bar.

Temperature	CO_2 partial pressure (p), mbar						
(ºC)	12	20	40	70	200	300	400
20	2.7	2.1	1.9	1.4	1.1	1.1	1.0
60	2.7	2.1	1.7	1.4	1.1	1.0	1.0
100	2.1	1.7	1.5	1.4	1.0	1.0	1.0

Supplementary Table 12. CO_2 transport properties based on the transport model. The model fitted K_{eq} and $k_{trans}(\rho)q_{max}$ was extracted from the temperature-dependent gas permeation measurement (Table S11). ΔH_{ad} and E_{act} are extracted from the temperature-dependent Arrhenius and Van 't Hoff equations, respectively.

Temperature (ºC)	K_{eq} (Pa^{-1})	$k_{trans}(\rho)q_{max}$ (mole m^{-2} s^{-1})	ΔH_{ad} (kJ $mole^{-1}$)	E_{act} (kJ $mole^{-1}$)
20	4.4×10^{-4}	2.0×10^{-3}		
60	1.5×10^{-4}	12.4×10^{-3}	-25.2	34.8
100	4.7×10^{-5}	42.2×10^{-3}		

Supplementary Table 13. CO_2/N_2 mixture separation performance comparison between the pyridinic-N-substituted graphene membranes presented in this work and state-of-the-art membranes. The data comparison is for postcombustion capture conditions where CO_2/N_2 mixture is used with CO_2 composition of 20%.

Membrane type	Material	CO_2 permeance (GPU)	CO_2/N_2 SF	Reference
Commercial	Cellulose acetate	110	30	[20]
	Polaris®	1000	50	[20]
Graphene oxide (GO)	GO with PEGDA	186	59	[28]
	GO with ionic liquid	37	130	[29]
	GO	103	18	[30]
Facilitated transport membranes	Piperazine modified GO	1020	680	[31]
	Enzymatic solution	2600	788	[32]
	Polyvinylamine	1827	500	[33]
	2-pyrrolidone & 2-methoxyethanol	908	162	[34]
	Polyvinylamine/amino acid salt	947	210	[35]
	Ionic liquid on graphene	4000	20	[36]
Carbon molecular sieve membranes	Fluorinated carbon molecular sieve membranes	29	36	[37]
Mixed matrix membranes	UiO-66-NH_2 in PEBAX®	338	57	[38]
	ZIF-8 in PEBAX®	345	32	[39]
	GO in thermally-reduced (TR) polymer	1784	18*	[40]
Hybrid membranes	Poly(ionic liquids)	132	27	[41]
	Metal-induced ordered microporous polymers (MMPs)	3000	78	[42]
Polymeric membranes	PEG/PDMS	1210	22	[43]
	PEG/NH_2-MIL-53	2600	14	[44]
	DAmPEG-TMC	1310	33	[45]
	Pebax2533/PEG-*b*-PPFPA	3330	22*	[46]
Porous single-layer graphene based membranes	Porous single-layer graphene	2933	39	[47]
		5857	28	
		11850	22	[24]
	Polymer-functionalized single-layer graphene	8714	23	[47]
		7277	22	
		8730	33	
	Pyridinic-N-substituted porous graphene	11570	60	Average data from 6 membranes in this work
		10420±1710	53.3±9.8	

* Indicates the ideal selectivity; PEGDA: Poly(ethylene glycol) diamines; PEG: Poly(ethylene glycol); PDMS: Polydimethylsiloxane; PEG-b-PPFPA: poly(ethylene glycol)-block-poly(pentafluoropropyl actylate); DAmPEG: diaminopolyethylene glycol; TMC: trimesoyl chloride; ZIF-8: zeolitic imidazolate frameworks; UiO: Universitetet i Oslo.

Supplementary References

1. Feng, Y., Xie, R., Wu, Z. & Marsh, K. N. Vapor−Liquid Equilibria for Ammonia + Methanol. *J. Chem. Eng. Data* **44**, 401–404 (1999).

2. Schäfer, D., Xia, J., Vogt, M., Pérez-Salado Kamps, Á. & Maurer, G. Experimental Investigation of the Solubility of Ammonia in Methanol. *J. Chem. Eng. Data* **52**, 1653–1659 (2007).

3. Beams, R., Gustavo Cançado, L. & Novotny, L. Raman characterization of defects and dopants in graphene. *J. Phys. Condens. Matter* **27**, 083002 (2015).

4. Wang, Q. H. *et al.* Understanding and controlling the substrate effect on graphene electron-transfer chemistry via reactivity imprint lithography. *Nat. Chem.* **4**, 724–732 (2012).

5. Froehlicher, G. & Berciaud, S. Raman Spectroscopy of Electrochemically-Gated Graphene Transistors: Geometrical Capacitance, Electron-Phonon, Electron-Electron, and Electron-Defect Scattering. *Phys. Rev. B* **91**, 205413 (2015).

6. Das, A. *et al.* Monitoring dopants by Raman scattering in an electrochemically top-gated graphene transistor. *Nat. Nanotechnol.* **3**, 210–215 (2008).

7. Wang, Z. *et al.* N-doped porous carbon derived from polypyrrole for CO2 capture from humid flue gases. *Chem. Eng. J.* **396**, 125376 (2020).

8. Yang, C. *et al.* Facile preparation of N-doped porous carbon from chitosan and NaNH2 for CO2 adsorption and conversion. *Chem. Eng. J.* **432**, 134347 (2022).

9. Yuan, Z. *et al.* Mechanism and Prediction of Gas Permeation through Sub-Nanometer Graphene Pores: Comparison of Theory and Simulation. *ACS Nano* **11**, 7974–7987 (2017).

10. Celebi, K. *et al.* Atomically Thin Porous Graphene. *Science* **344**, 289–293 (2014).

11. Dakhchoune, M. *et al.* Rapid Gas Transport from Block-Copolymer Templated Nanoporous Carbon Films. *Ind. Eng. Chem. Res.* **60**, 16100–16108 (2021).

12. Jiao, Y., Zheng, Y., Smith, S. C., Du, A. & Zhu, Z. Electrocatalytically Switchable CO2 Capture: First Principle Computational Exploration of Carbon Nanotubes with Pyridinic Nitrogen. *ChemSusChem* **7**, 435–441 (2014).

13. Luan, B. *et al.* Crown Nanopores in Graphene for CO2 Capture and Filtration. *ACS Nano* **16**, 6274–6281 (2022).

14. Zhao, Y., Liu, X., Yao, K. X., Zhao, L. & Han, Y. Superior Capture of CO2 Achieved by Introducing Extra-framework Cations into N-doped Microporous Carbon. *Chem. Mater.* **24**, 4725–4734 (2012).

15. Lim, G., Lee, K. B. & Ham, H. C. Effect of N-Containing Functional Groups on CO2 Adsorption of Carbonaceous Materials: A Density Functional Theory Approach. *J. Phys. Chem. C* **120**, 8087–8095 (2016).

16. Wang, L. *et al.* Fundamental transport mechanisms, fabrication and potential applications of nanoporous atomically thin membranes. *Nat. Nanotechnol.* **12**, 509–522 (2017).

17. Micari, M., Dakhchoune, M. & Agrawal, K. V. Techno-economic assessment of postcombustion carbon capture using high-performance nanoporous single-layer graphene membranes. *J. Memb. Sci.* **624**, 119103 (2021).

18. Pan, C. Y. Gas separation by permeators with high-flux asymmetric membranes. *AIChE J.* **29**, 545–552 (1983).

19. Shindo, Y., Hakuta, T. & Yoshitome, H. Calculation Methods for Multicomponent Gas Separation by Permeation. *Sep. Sci. Technol.* **20**, 445–459 (1985).

20. Merkel, T. C., Lin, H., Wei, X. & Baker, R. Power plant post-combustion carbon dioxide capture: An opportunity for membranes. *J. Memb. Sci.* **359**, 126–139 (2010).

21. Roussanaly, S., Anantharaman, R., Lindqvist, K., Zhai, H. & Rubin, E. Membrane properties required for post-combustion CO2 capture at coal-fired power plants. *J. Memb. Sci.* **511**, 250–264 (2016).

22. Han, Y. & Ho, W. S. W. Facilitated transport membranes for H2 purification from coal-derived syngas: A techno-economic analysis. *J. Memb. Sci.* **636**, 119549 (2021).

23. Ramasubramanian, K., Verweij, H. & Winston Ho, W. S. Membrane processes for carbon capture from coal-fired power plant flue gas: A modeling and cost study. *J. Memb. Sci.* **421**–**422**, 299–310 (2012).

24. Huang, S. *et al.* Millisecond lattice gasification for high-density CO2- and O2-sieving nanopores in single-layer graphene. *Sci. Adv.* **7**, eabf0116 (2021).

25. Vacchi, I. A., Spinato, C., Raya, J., Bianco, A. & Ménard-Moyon, C. Chemical reactivity of graphene oxide towards amines elucidated by solid-state NMR. *Nanoscale* **8**, 13714–13721 (2016).

26. Wang, W.-W., Dang, J.-S., Zhao, X. & Nagase, S. Formation Mechanisms of Graphitic-N: Oxygen Reduction and Nitrogen Doping of Graphene Oxides. *J. Phys. Chem. C* **120**, 5673–5681 (2016).

27. Park, H. B., Kamcev, J., Robeson, L. M., Elimelech, M. & Freeman, B. D. Maximizing the right stuff: The trade-off between membrane permeability and selectivity. *Science* **356**, eaab0530 (2017).

28. Wang, S. *et al.* Graphene Oxide Membranes with Heterogeneous Nanodomains for Efficient CO2 Separations. *Angew. Chemie Int. Ed.* **56**, 14246–14251 (2017).

29. Karunakaran, M. *et al.* Graphene oxide doped ionic liquid ultrathin composite membranes for efficient CO2 capture. *J. Mater. Chem. A* **5**, 649–656 (2017).

30. Kim, H. W. *et al.* Selective Gas Transport Through Few-Layered Graphene and Graphene Oxide Membranes. *Science* **342**, 91–95 (2013).

31. Zhou, F. *et al.* Ultrathin graphene oxide-based hollow fiber membranes with brush-like CO2-philic agent for highly efficient CO2 capture. *Nat. Commun.* **8**, 2107 (2017).

32. Fu, Y. *et al.* Ultra-thin enzymatic liquid membrane for CO2 separation and capture. *Nat. Commun.* **9**, 990 (2018).

33. Kim, T.-J., Vrålstad, H., Sandru, M. & Hägg, M.-B. Separation performance of PVAm composite membrane for CO2 capture at various pH levels. *J. Memb. Sci.* **428**, 218–224 (2013).

34. Pang, R., Chen, K. K., Han, Y. & Ho, W. S. W. Highly permeable polyethersulfone substrates with bicontinuous structure for composite membranes in CO2/N2 separation. *J. Memb. Sci.* **612**, 118443 (2020).

35. Zhang, Z., Rao, S., Han, Y., Pang, R. & Ho, W. S. W. CO2-selective membranes containing amino acid salts for CO2/N2 separation. *J. Memb. Sci.* **638**, 119696 (2021).

36. Guo, W., Mahurin, S. M., Unocic, R. R., Luo, H. & Dai, S. Broadening the Gas Separation Utility of Monolayer Nanoporous Graphene Membranes by an Ionic Liquid Gating. *Nano Lett.* **20**, 7995–8000 (2020).

37. Yang, Z. *et al.* Surpassing Robeson Upper Limit for CO2/N2 Separation with Fluorinated Carbon Molecular Sieve Membranes. *Chem* **6**, 631–645 (2020).

38. Sutrisna, P. D. *et al.* Surface functionalized UiO-66/Pebax-based ultrathin composite hollow fiber gas separation membranes. *J. Mater. Chem. A* **6**, 918–931 (2018).

39. Sutrisna, P. D., Hou, J., Li, H., Zhang, Y. & Chen, V. Improved operational stability of Pebax-based gas separation membranes with ZIF-8: A comparative study of flat sheet and composite hollow fibre membranes. *J. Memb. Sci.* **524**, 266–279 (2017).

40. Kim, S. *et al.* Highly permeable thermally rearranged polymer composite membranes with a graphene oxide scaffold for gas separation. *J. Mater. Chem. A* **6**, 7668–7674 (2018).

41. Nikolaeva, D. *et al.* Poly(vinylbenzyl chloride)-based poly(ionic liquids) as membranes for CO2 capture from flue gas. *J. Mater. Chem. A* **5**, 19808–19818 (2017).

42. Qiao, Z. *et al.* Metal-induced ordered microporous polymers for fabricating large-area gas separation membranes. *Nat. Mater.* **18**, 163–168 (2019).

43. Fu, Q. *et al.* A novel cross-linked nano-coating for carbon dioxide capture. *Energy Environ. Sci.* **9**, 434–440 (2016).

44. Xie, K. *et al.* Continuous assembly of a polymer on a metal-organic framework (CAP on MOF): A 30 nm thick polymeric gas separation membrane. *Energy Environ. Sci.* **11**, 544–550 (2018).

45. Li, S. *et al.* Interfacially polymerized thin film composite membranes containing ethylene oxide groups for CO2 separation. *J. Memb. Sci.* **436**, 121–131 (2013).

46. Scofield, J. M. P. *et al.* Development of novel fluorinated additives for high performance CO2 separation thin-film composite membranes. *J. Memb. Sci.* **499**, 191–200 (2016).

47. Hsu, K.-J. *et al.* Multipulsed Millisecond Ozone Gasification for Predictable Tuning of Nucleation and Nucleation-Decoupled Nanopore Expansion in Graphene for Carbon Capture. *ACS Nano* **15**, 13230–13239 (2021).